DETERMINATION OF FLAME CHARACTERISTICS IN A LOW SWIRL BURNER AT GAS TURBINE CONDITIONS THROUGH REACTION ZONE IMAGING

A Dissertation
Presented to
The Academic Faculty

by

Karthik Periagaram

In Partial Fulfillment
of the Requirements for the Degree
Doctor of Philosophy in the
Guggenheim School of Aerospace Engineering

Georgia Institute of Technology
December 2012

TABLE OF CONTENTS

LIST OF FIGURES

LIST OF TABLES

LIST OF SYMBOLS

X_f Flame standoff distance

SUMMARY

CHAPTER 1

INTRODUCTION

1.1 Motivation

The need to reduce pollutant emissions, particularly the oxides of nitrogen, NO_x, in order to meet increasingly stringent government regulations spurs efforts in the gas turbine industry to seek cleaner, more environment-friendly combustion concepts. The production rate of NO_x is highly temperature dependent and fuel-lean, premixed combustion is a widely employed technique to keep the adiabatic flame temperature under 1800 K. However, operating a combustor at such lean conditions results in eaker combustion processes that are highly susceptible to perturbations and combustor instabilities. This highlights the requirements for robust flame stabilization techniques to sustain combustion at ultra-lean conditions. The Low Swirl Burner (LSB) design addresses these requirements by providing a low NO_x combustor that can operate stably at lean equivalence ratios.

In typical hydrocarbon-air flames, CH is produced and destroyed rapidly by fast two-body reactions, confining it to the thin heat release zone of the flame. This has led to the widespread use of using CH as a marker species for the flame front.[1] CH is formed during the breakup of hydrocarbon fuel molecules[2] and is also known to play an important role in the production of prompt NO_x.[3] Hence, it is a minor species of considerable importance to combustion research.

This study primarily utilizes CH PLIF as a flame visualization technique. Broadly speaking, flame visualiation techniques could be grouped into two categories: techniques that convey spatially integrated information about the flame and techniques that resolve the information spatially. Schlieren or chemiluminescence imaging of

flames fall in the former category, providing line-of-sight averaged information about the flame. Planar LIF or typical implementations of Rayleigh/Raman scattering are examples of the second category.

PLIF studies of hydrocarbon flames have hitherto focused on the OH radical. OH is produced in the flame zone and destroyed by relatively slow three-body reactions, causing it to persist and be transported away from the flame and into the product zone.[4] As a result, it does not serve as a direct marker of the flame front. Instead, the location of the flame is inferred from the sharp gradient in the OH signal as the reactants are converted into products.

Due to the persistence of OH in the products, OH PLIF is somewhat less suited to studying flows with high product recirculation. In such flows, the presence of OH both in the reactants and in the products weakens the gradient at the flame. Further, OH radicals can be transported transverse to the flame, making it difficult to detect local flame extinctions. Nevertheless, researchers have been able to use OH PLIF to study such flames,[5, 6] particularly when the images are enhanced by nonlinear filtering techniques.[7, 8]

Recent studies[9] have indicated that the species HCO is a superior indicator of heat release in hydrocarbon flames when compared to CH or OH. The HCO LIF signal has been demonstrated to correlate well with the heat release rate, with little dependence on equivalence ratio or strain rate. The last factor, in particular, has been shown to quench the CH PLIF signal[10] in highly strained flames, even when the flame itself is not extinguished. Unfortunately, the signal levels from HCO LIF are very poor[9, 11] and are unsuitable for single-shot investigation of hydrocarbon flames. To overcome this, one study[11] proposed a simultaneous LIF investigation of CH_2O and OH with the reasoning that the formation rate of HCO is governed directly by the product of the concentration of these two intermediates. This method has been used in a number of investigations, despite being experimentally cumbersome. A

2

later implementation[12] recently demonstrated single-shot HCO PLIF with moderate signal-to-noise ratios by utilizing a novel excitation scheme.

item Nearly resonant PLIF. Excite A(0,0) band, observe A(0,0). item Excite B(0,0), observe A(0,0) subitem Excite Q lines. subitem Excite R lines / bandhead.

CHAPTER 2

BACKGROUND

2.1 LSB flow field

2.2 LSB flame stabilization

2.3 CH PLIF Physical Description

Laser-Induced Fluorescence, or LIF, is a two-step process. First, a marker species molecule (in this case, CH) in a lower energy state absorbs a photon and transitions to a higher energy state. The photon in question is provided by a laser and is of a specific energy (or frequency) chosen to match an allowed transition in the target species. This is followed by several physical processes, of which one pathway of interest leads to the spontaneous deexcitation of the excited molecule, accompanied by the release of a photon. The dexcitation may take the molecule back to the original ground state or to another energy state. The choice of the spectral and temporal properties of the excitation photon and the spontaneously emitted photon, together constitute the excitation scheme.

The excitation scheme chosen for this study follows the work done by Li et al.[13] who used a ring-cavity, pulsed alexandrite laser to provide excitation in the vicinity of the R-bandhead of the CH $B^2\Sigma^- \leftarrow X^2\Pi$ (0,0) system. This bandhead is found at about 387.2 nm and represents transitions from a ground state rotational quantum number of $N'' = 7$. Alexandrite lasers have relatively large bandwidths (a few cm^{-1} is not uncommon) and hence make it possible to excite several of the neighboring transitions near the bandhead. From simulations described later in this work, it is found that CH molecules in the ground state $X^2\Pi$, $v'' = 0$ with rotational quantum

numbers N'' between 5–9 account for virtually all the absorption that takes place.

Upon excitation, these molecules transition to the second electronically excited $B^2\Sigma^-$ state and populate the ground state vibrational level ($v' = 0$). Since these transitions are in the R-branch, the rotational quantum number increases by $+1$, resulting in the population of the N'' levels between 6–10. Now, the following possibilities exist for the excited molecule:

1. The molecule can undergo inelastic collisions with other molecules, resulting in relaxation in the rotational, vibrational or electronic manifolds.

2. The molecule can spontaneously emit a photon and return to any of the lower energy states.

3. The molecule can experience stimulated emission in the presence of another photon of the appropriate frequency and return to any of the lower energy states.

4. The molecule can experience further excitation either by absorbing a photon or through collisional means.

5. The molecule, having enough activation energy, can react chemically with another species.

Now, let us examine these potential pathways in greater detail. The first pathway pertains to relaxation. The excitation and subsequent population of a higher energy state causes the CH population distribution to deviate from the equilbrium Boltzmann distribution. The degree of relaxation possible is limited by the lifetime of the energy level the excited species occupy. The collision-free, radiative lifetime of the B electronic state is about 300 ns[14]—long enough for sufficient rotational relaxation to occur, but too short for vibrational relaxation. As a result, we may suppose that the vibrational manifold remains relatively unaffected, while the rotational manifold is

5

relaxed closer to an equilibrium distribution. The question of the electronic relaxation will be addressed later in this discussion.

The second option available for the excited CH molecule is to spontaneously emit a photon and return to a lower energy state. The CH system is very strongly diagonal, meaning that transitions resulting in no change to the vibrational quantum number are extremely favored over others. This means the majority of this spontaneous emission will result from $B^2\Sigma^- \rightarrow X^2\Pi(0,0)$ and $B^2\Sigma^- \rightarrow A^2\Delta(0,0)$ deexcitations. The $B \rightarrow X$ transition will be nearly resonant with the excitation wavelength, making it hard to observe, while the $B \rightarrow A$ transition is only a few hundred wavenumbers apart, putting the emission in far IR. Even setting the difficulty of observing these transitions aside, it is not expected that a significant portion of the excited CH molecules would follow these pathways as it requires an excited CH molecule to remain collision-free for far too long.

The third option is for the CH molecule to experience stimulated emission in the presence of a photon of an appropriate frequqncy. It is highly unlikely that the apposite photon would have a frequency other than the excitation laser. The incident laser beam with induce some stimulated emission and deexcite a portion of the CH molecules back through the $B^2\Sigma^- \rightarrow X^2\Pi(0,0)$ transition to the ground state. The only other sources of light in the frequencies of interest result from other CH molecules. Some of these photons will originate from CH* chemiluminescence, while others still will be produced by the laser-induced fluorescence between the $B \rightarrow X$ states.

As alluded to earlier, it is highly unlikely that these will result in stimulated emission of significant proportions. Partly, this is due to the spatial distribution of CH in a typical combustion environment. As mentioned earlier in Chapter FIXME 1, CH molecules are expected to be found only in the very thin reaction zone of the flame. Further, CH is a minor species and not likely to be found in concentrations in excess of a few parts per million. This makes is rather unlikely that a spontaneously emitted

photon from another CH molecule would encounter another excited CH molecule and 131
induce a stimulated emission pathway. In other words, we expect the medium to 132
be optically thin to the wavelengths of interest. We will return to this concept of 133
an optically thin medium in a subsequent section while modeling the CH absorption 134
strength. 135

The fourth option is for the molecule to experience further excitation from absorb- 136
ing another photon or through collisions with other energetic molecules. The $B^2\Sigma^-$ 137
state is very shallow, possessing only two vibrational levels before the molecule will 138
dissociate. Thus, this pathway leads to predissociation of the excited CH molecule. 139

The final option listed above is for the excited CH molecule to attack another 140
species and participate in chemical reactions. If the reaction would not have occurred 141
had the CH molecule been in its ground state, this is referred to as a laser-induced 142
chemical reaction. 143

Having listed all the options, let's return to the first option and resume the dis- 144
cussion on the possibility of electronic energy transfer from the excited $B^2\Sigma^-$, $v' = 0$ 145
state. The spacing of the energy levels in the CH system is such that the $B^2\Sigma^-$, 146
$v' = 0$ state is found to be near-degenerate with the $A^2\Delta$, $v = 1$ energy level. Con- 147
sequently, the $B^2\Sigma^- \leftrightarrow A^2\Delta$ (0,1) transition is reversible. Further, recall that CH is 148
a strongly diagonal system with high transition probabilities for transitions involving 149
no change to the vibrational quantum number. This means that the $B^2\Sigma^- \leftrightarrow A^2\Delta$ 150
(0,0) transition will be quite strong as well. Experiments performed by Garland et 151
al.[15] measured that the $B^2\Sigma^- \to A^2\Delta$ electronic energy transfers account for almost 152
a quarter of all collisional depletion of the $B^2\Sigma^-$, $v = 0$ level. 153

Theoretical calculations using overlap integrals between the involved energy levels 154
predict that a majority of these transfers will be along the diagonal (0,0) transition.[16]. 155
Instead, experimental data indicates that the number is closer to a fifth, with almost 156
80% of the transfers following the near-degenerate (0,1) pathway. It is this electronic 157

energy transfer mechanism that enables our excitation scheme to record high quality CH PLIF images. Having now populated the $A^2\Delta$ states, the resulting spontaneous emission from the $A^2\Delta \to X^2\Pi$ (0,0) and (1,1) transitions can be easily observed between 420–440 nm. A small portion of the fluorescence in this wavelength range also occurs from the $B^2\Sigma^- \to X^2\Pi$, (0,1) transition. Since these emission wavelengths are at least 30 nm away from the excitation wavelength, a simple glass filter is sufficient to suppress any elastic scattering from the laser beam.

2.4 CH PLIF Signal Modeling

We now focus on developing a mathematical model to predict the signal levels obtained from CH PLIF. The intent and scope of this discussion is to be able to predict, in a semi-quantitative manner, the variation of the CH PLIF signal as a function of the thermodynamic state variables and the local composition in the reaction zone of a flame. It is not meant to be an accurate calculation of the number of LIF photons produced in a given experiment. This prediction will allow us to compare the PLIF signal intensity across various initial pressures, temperatures and reactant mixtures. The results will enable us to judge the feasibility of using CH PLIF as a diagnostic technique to image the flame front with high fidelity for the initial conditions and reactant mixtures in question.

2.4.1 Basic Model

In its most basic form, the number of fluorescence photons generated in a system, Φ is the product of the number of emitters, N and the Einstein coefficient for spontaneous emission, A.

$$\Phi = N \times A \tag{2.1}$$

8

In a simple two-level model for the fluorescing system (with the two levels labeled 0 and 1), Equation 2.1 may be expanded in terms of the number density of the emitters, n and the volume in which the fluorescence occurs, V.

$$\Phi = n_1 V A_{10} \tag{2.2}$$

The population of the upper state, n_1 can be solved for by rate analysis. The mathematical treatment is not particularly complicated and is covered in detail by various textbooks and review papers.[17] Here, we shall merely remark that the functional form of the solution has two limiting cases. The limits are decided by the relative magnitudes of the pumping rate, W_{01} and the relaxation rate given by the sum of the spontaneous emission rate and the collisional quenching rate, $A_{10} + Q_{10}$. The former is the rate at which the upper energy level is populated through absorption. The latter represents the rate at which the molecules return to the lower energy state, either through spontaneous emission or by losing energy to other molecules through inelastic collisions.

When the pumping rate is far lower compared to the relaxation processes ($W_{01} \ll A_{10} + Q_{10}$), the solution tends to the weak excitation limit. In this limit, the functional form of the solution is shown in Equation 2.3

$$\Phi = n_0 V W_{01} \; \overbrace{\frac{A_{10}}{A_{10} + Q_{10}}}^{\text{Fluorescence Yield}} \tag{2.3}$$

The $n_0 V W_{01}$ term in Equation 2.3 represents the number of molecules that are excited to the upper state per second, while the fluorescence yield represents the fraction of these molecules that will produce a LIF signal. In typical combustion environments, the fluorescence yield is usually small, since the collisional quenching rate dominates the spontaneous emission rate. The rate of collisional quenching of the marker species, in this case CH, by another species in the flame is proportional

9

to the frequency of collisions between the two species. Further, the effectiveness of such collisions is decided by a collision cross-section, σ, which is often a function of the temperature. Equation 2.4 presents the calculation of the collisional quenching rate by summation over all the species, i, in the flame.

$$
\begin{aligned}
Q_{10} &= \sum_i n_i \times \sigma_i \times c_i \\
&= \sum_i n_i \sigma_i \sqrt{\frac{8kT}{\pi \mu_i}} \\
&= \sqrt{\frac{8kT}{\pi}} \sum_i \frac{n_i \sigma_i}{\sqrt{\mu_i}}
\end{aligned}
\tag{2.4}
$$

In Equation 2.4, μ_i represents the reduced mass of the colliding CH-i molecules, p is the pressure, N_A is Avogadro's Number, R is the Universal Gas Constant, T is the temperature, and n_i is the number density of species i. The expression for the reduced mass is given in Equation 2.5.

$$
\mu_i = \frac{m_i m_{CH}}{m_i + m_{CH}}
\tag{2.5}
$$

By probability, virtually all the collisions of the CH molecule will occur with the major species. As a result, the summation in Equation 2.4 need only be carried out over the major species in the flame. The values of the local number densities of the major species can be measured by techniques like Raman scattering, or can be obtained from solving chemical kinetics models.

2.4.1.1 Absorption Integral Calculation

Let us now examine the first term in Equation 2.3 in further detail. Let $\phi(\nu)$ represent the normalized lineshape of the absorption line being excited, such that $\int \phi(\nu)d\nu = 1$. If B_{01} is the Einstein coefficient for absorption for the line being excited, the term

10

$B_{01}\phi(\nu)$ represents the spectral absorptivity of the line at ν. B_{01} is usually presented in m^2/Js for LIF applications. Similarly, let I_ν be the spectral intensity of the incident radiation, which is the intensity (power per area) of the laser beam per spectral interval. Let $\psi(\nu)$ be the normalized spectral profile of the laser lineshape, such that $I_\nu = I\psi(\nu)$ and $\int \psi(\nu)d\nu = 1$. I_ν is usually given in W/cm^2/cm^{-1} for ease of use in laser applications.

The product of the spectral absorptivity and the spectral intensity integrated over the spectrum, gives the pumping rate, W_{01} as shown in Equation 2.7. The factor c is the speed of light, which brings the units of W_{01} to s^{-1}.

$$W_{01} = \frac{I}{c} \int \psi(\nu) B_{01}\phi(\nu)d\nu \tag{2.6}$$

Since our excitation scheme targets multiple lines in the R-bandhead, we actually have a summation of several absorption lines in this integral.

$$
\begin{aligned}
W_{01} &= \frac{I}{c} \int \psi(\nu) \sum_j B_j\phi_j(\nu)d\nu \\
&= \frac{I}{c} \sum_j \int B_j\psi(\nu)\phi_j(\nu)d\nu
\end{aligned}
\tag{2.7}
$$

In Equation 2.7, the terms B_j are the absorption coefficients, B_{01}, for each transition being excited. Consider now, each term in the above integral. The laser lineshape function, $\psi(\nu)$, can be modeled as a Gaussian profile without any loss of generality. The linewidth of the alexandrite laser, when operated in broadband mode is of the order of a few wavenumbers. The effect of line broadening mechanisms, such as natural broadening, inhomogeneous broadening, etc that are commonly encountered in solid state lasers are negligible in comparison and hence, do not affect the lineshape

appreciably.

$$\psi(\nu) = \frac{1}{\sigma_l\sqrt{2\pi}} \exp\left(-\frac{(\nu - \nu_l)^2}{2\sigma_l^2}\right) \tag{2.8}$$

The mean of the lineshape profile, ν_l, is set by tuning the center wavelength of the laser. The Full Width at Half Max (FWHM) of the laser, $\Delta\nu_l$, is prescribed by the manufacturer and can be used to calculate the standard deviation of the Gaussian as follows.

$$\sigma_l = \frac{\Delta\nu_l}{2\sqrt{2\ln 2}} \tag{2.9}$$

The lineshape of the absorption line being excited, on the other hand, is primarily dictated by mechanisms associated with gas-phase media—collisional broadening and Doppler broadening being the most important ones. Collisional broadening is a ho- mogeneous mechanism and produces a Lorentzian broadened lineshape. The FWHM of the Lorentzian profile is related to the thermodynamic conditions by the following empirical formula.

$$\Delta\nu_c = 0.1\left(\frac{p}{p_0}\right)\left(\frac{T_0}{T}\right)^{0.6} \tag{2.10}$$

In Equation 2.10, p_0 and T_0 represent standard conditions of pressure and tem- perature (101325 Pa and 300 K) respectively. By contrast, Doppler broadening is an inhomogenous mechanism that results in a Gaussian lineshape. Its effect depends on the frequency (wavenumber) of the line being broadened, ν_a, and on the molecule's velocity. The FWHM of the resulting broadened lineshape is given by,

$$\Delta\nu_d = \nu_a\frac{\ln 2}{c}\sqrt{\frac{8kT\ln 2}{m_C H}} \tag{2.11}$$

The combined effect of these two broadening mechanisms can be calculated by

convoluting the two broadened lineshapes. In this case, a Lorentzian convoluted with a Gaussian results in a Voigt profile. In order to simplify the calculations, we assume that the collision-broadened Lorentzian profile is reasonably approximated by a Gaussian profile with the same FWHM. Now, the convolution of the two profiles results in another Gaussian, with the same mean and a FWHM given by,

$$\Delta\nu_a = \sqrt{\Delta{\nu_c}^2 + \Delta{\nu_d}^2} \tag{2.12}$$

Thus, the Gaussian lineshape of the broadened absorption line can be written as,

$$\phi(\nu) = \frac{1}{\sigma_a\sqrt{2\pi}}\exp\left(-\frac{(\nu - \nu_a)^2}{2\sigma_a^2}\right) \tag{2.13}$$

In Equation 2.13, ν_a is the frequency (wavenumber) of the absorption peak being excited. The standard deviation of the lineshape, σ_a, is related to the broadened FWHM, $\Delta\nu_a$, by the following equation.

$$\sigma_a = \frac{\Delta\nu_a}{2\sqrt{2\ln 2}} \tag{2.14}$$

With the above information, the integral in Equation 2.7 can be solved analytically as follows.

$$\int \psi(\nu)\phi(\nu)d\nu = \frac{1}{\sqrt{2\pi(\sigma_a^2 + \sigma_l^2)}}\exp-\frac{(\nu_l - \nu_a)^2}{2(\sigma_a^2 + \sigma_l^2)} \tag{2.15}$$

2.4.1.2 Population distribution

Once again, consider Equation 2.3, this time focusing on the term n_0, the number density of the marker species (CH, in this case) in the lower energy state that are available for excitation to the upper state. This comprises only a small subset of all

the available CH molecules in the flame.

$$n_0 = n f_j \tag{2.16}$$

The fraction, f_j, of CH molecules that populate the energy level j can be calculated from the Boltzmann distribution. Equation 2.17 presents the expression for f_j in terms of the vibrational and rotational quantum numbers, (v, J), of the energy level j.

$$f(v, J) = \frac{\exp\left(\dfrac{-hcE_v(v)}{kT}\right)(2J+1)\exp\left(\dfrac{-hcE_r(v, J)}{kT}\right)}{Q_{rv}} \tag{2.17}$$

The vibrational energy, $E_v(v)$ of a level is calculated according to Equation 2.18, while the rotational energy, $E_r(v, J)$ is calculated according to Equation 2.19.

$$E_v(v) = \omega_e\left(v + \frac{1}{2}\right) - \omega_e x_e\left(v + \frac{1}{2}\right)^2 + \omega_e y_e\left(v + \frac{1}{2}\right)^3 - \omega_e z_e\left(v + \frac{1}{2}\right)^4 \tag{2.18}$$

$$E_r(v, J) = \left\{B_e - \alpha_e\left(v + \frac{1}{2}\right)\right\}J(J+1) - \left\{D_e + \beta_e\left(v + \frac{1}{2}\right)\right\}J^2(J+1)^2 \tag{2.19}$$

The spectroscopic constants in Equations 2.18 and 2.19 can be found in literature[18].

The rovibrational partition function, Q_{rv} is a summation over all available vibra- tional and rotational levels in the particular electronic state. For the ground state of the CH molecule, there are five available vibrational quantum numbers, $v = 0$ to $v = 4$. The $B^2\Sigma^- \leftarrow X^2\Pi$ transition of the CH system is governed by Hund's Case b and hence, the appropriate rotational quantum number to use is N. Each vibrational level has twenty-two possible values for N from $N = 1$ to $N = 22$. For each rotational quantum number N, there are two possible values of J given by $N \pm \frac{1}{2}$.

2.4.1.3 Solution

Substituting Equations 2.7 and 2.16 into 2.3, and noting that the signal produced is
actually integrated over a volume,

$$\Phi = \int_V \frac{nA_{10}}{A_{10} + Q_{10}} \frac{I}{c} \sum_j f_j B_j \int_\nu \psi(\nu)\phi_j(\nu)d\nu dV \tag{2.20}$$

In Equation 2.20, the absorption integral from Equation 2.15 is highlighted in red.
The outer integral is performed in space, over the portion of the flame illuminated by
the laser sheet. It is possible to rewrite the outer integral as a 1-D integral over the
thickness of the flame by replacing the laser intensity, I with the laser power, P.

$$\Phi = \frac{P}{c} \int_x \frac{nA_{10}}{A_{10} + Q_{10}} \sum_j f_j B_j \int_\nu \psi(\nu)\phi_j(\nu)d\nu dx \tag{2.21}$$

Equation 2.21 is thus, the solution to the two-level model in the weak excitation
limit. Note that the LIF signal varies linearly as the incident laser power (or intensity).
Consequently, the weak excitation limit is also referred to as the linear regime.

For the sake of completion, the other limit of the two-level model solution occurs
when the rate of pumping far exceeds the relaxation rate ($W_{01} \gg A_{10} + Q_{10}$). This is
called the saturated limit and in this limit, the fluorescence signal no longer depends
on the intensity of the incident laser beam. Operating in this regime is generally not
preferred as the saturation criterion is difficult to satisfy simultaneously in the spatial,
temporal and spectral domains. For this reason, we will restrict our discussion hence
forward the linear regime only.

2.4.2 Improved Model

While the two-level model is conceptually simple, applying it to describe complicated
systems, such as the CH molecule, results in large errors.[17] Hence, it is worthwhile
to investigate a more complicated model that can describe the CH system with higher
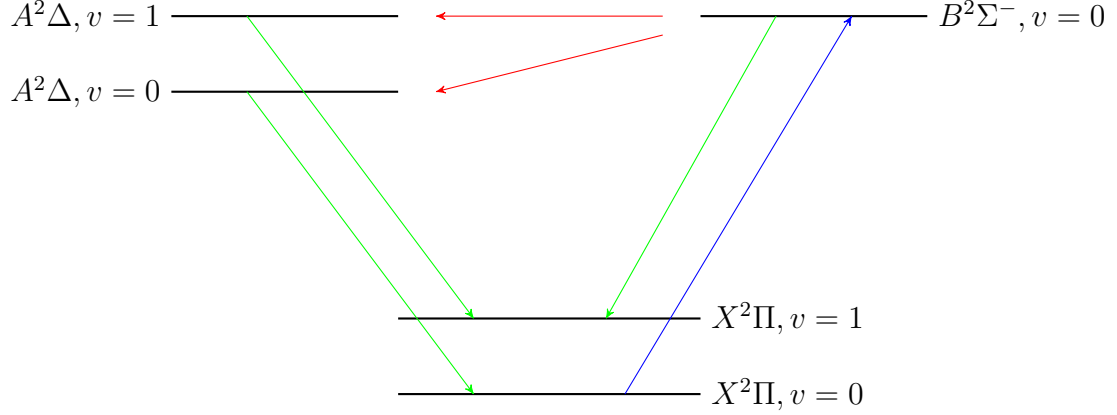
Figure 2.1: *Some of the important transitions between energy levels in a CH molecule are shown. The excitation of the CH molecules (blue) is followed by collisional energy transfer processes (red) which populate additional energy levels. Spontaneous emission from some of these energy levels (green) is collected.*

fidelity.

Figure 2.1 shows the pathways described in Section FIXME. An accurate model of the CH system should involve at least five energy levels, namely the $B^2\Sigma^-$, $v = 0$, $A^2\Delta$, v=0,1, and $X^2\Pi$, v=0,1 levels. The model will need to account for collisional transfers between each of these levels, in addition to spontaneous and stimulated transitions. The mathematical solution quickly becomes tedious and complicated. Further, it involves several rate coefficients that have not yet been measured experimentally.

Fortunately, this can be significantly simplified. Previous studies[14, 16] have indicated that the off-diagonal $B \rightarrow X$ (0,1) transition plays a relatively minor role accounting for only 3.5% of the total fluorescence. Further, the $A \rightarrow X$ transitions are known[19] to be strongly diagonal, with little or no interaction[15] between the two states. The net result of these two assertions is that we can treat the two $B \rightarrow A \rightarrow X$ pathways to be disjoint and parallel. The resulting pseudo-three-level model is shown in Figure 2.2.

The rates of the various transition processes are indicated in Figure 2.2. W_{02} is the pumping process that populates the $B(0)$ state. Q_{ij} are collisional energy transfer

16
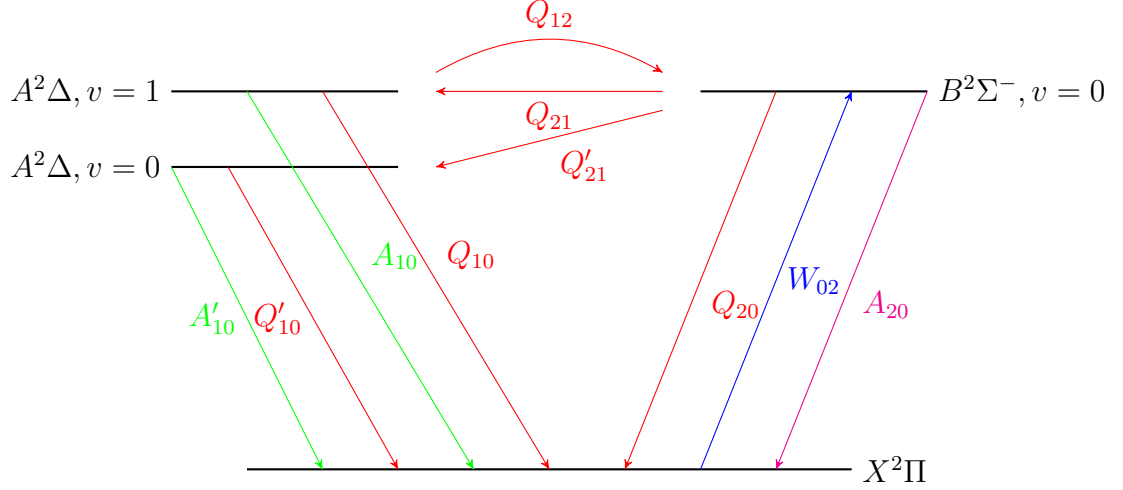
Figure 2.2: *A simplified model of the transitions between the energy levels in a CH system. Excitation (blue) of ground state CH molecules to the upper electronic state is followed by several collisional energy transfer processes (red). A small portion of these molecules spontaneously emit a photon (green) and return to ground state. The spontaneous emission corresponding to resonant PLIF (magenta) is not collected.*

processes that transfer CH molecules from the i level to the j level. The subscripts 0, 1 and 2 represent the electronic energy levels X, A and B. Processes involving the $A(0)$ state are differentiated from those involving the $A(1)$ state by a prime ($'$). Finally, A_{ij} represents the spontaneous emission coefficients between the i and j levels.

Applying Equation 2.1 to this case, we can write an expression for the LIF signal intensity as follows,

$$\Phi = (n_1 A_{10} + n_1' A_{10}')V \tag{2.22}$$

Our task is to solve for the values of n_1 and n_1' in terms of n_0. To do this we need to write rate equations describing the variation of the populations of the three upper states with time.

$$\frac{dn_1}{dt} = -(A_{10} + Q_{10} + Q_{12})n_1 + Q_{21}n_2 \tag{2.23}$$

$$\frac{dn_1'}{dt} = -(A_{10}' + Q_{10}')n_1' + Q_{21}'n_2 \tag{2.24}$$

$$\frac{dn_2}{dt} = W_{02}n_0 + Q_{12}n_1 - (A_{20} + Q_{20} + Q_{21} + Q_{21}')n_2 \tag{2.25}$$

Under the assumption that the laser excitation time scale is much longer that $\;\;\;$ 331
the collisional time scales, we can set the LHS of Equations 2.23–2.25 to zero. This $\;\;\;$ 332
results in a closed set of linear equations, which can be expressed in matrix form as $\;\;\;$ 333
follows. $\;\;\;$ 334

$$\begin{bmatrix} A_{10} + Q_{10} + Q_{12} & 0 & -Q_{21} \\ 0 & A_{10}' + Q_{10}' & -Q_{21}' \\ -Q_{12} & 0 & A_{20} + Q_{20} + Q_{21} + Q_{21}' \end{bmatrix} \begin{bmatrix} n_1 \\ n_1' \\ n_2 \end{bmatrix} = \begin{bmatrix} 0 \\ 0 \\ W_{02}n_0 \end{bmatrix} \tag{2.26}$$

From Equation 2.26, we only need the solutions to n_1 and n_1'. These solutions are $\;\;\;$ 335
presented in Equations 2.27–2.28. $\;\;\;$ 336

$$n_1 = n_0 W_{02} F \tag{2.27}$$

$$n_1' = n_0 W_{02} F' \tag{2.28}$$

. $\;\;\;$ 337

The expressions for the respective flourescence yields, F and F' are as follows, $\;\;\;$ 338

$$F = \frac{Q_{21}}{(A_{10} + Q_{10} + Q_{12})(A_{20} + Q_{20} + Q_{21} + Q'_{21}) - Q_{12}Q_{21}} \tag{2.29}$$

$$F' = \frac{(A_{10} + Q_{10} + Q_{12})Q'_{21}}{(A'_{10} + Q'_{10})((A_{10} + Q_{10} + Q_{12})(A_{20} + Q_{20} + Q_{21} + Q'_{21}) - Q_{12}Q_{21})} \tag{2.30}$$

2.4.2.1 Solution

Substituting the expressions from Equations 2.27–2.28 into Equation 2.22,

$$\Phi = n_0 V W_{02}(F + F') \tag{2.31}$$

Note the similarity in the form of Equation 2.31 to Equation 2.3. Both expressions are composed of two parts—a pumping rate and a fluorescence yield. Expanding the pumping rate W_{02} in a manner identical to Equation 2.7 and using the absorption integral in Equation 2.15, we can rewrite Equation 2.31 in a form mirroring Equation 2.21

$$\Phi = \frac{P}{c} \int_x n(F + F') \sum_j f_j B_j \int_\nu \psi(\nu)\phi_j(\nu)d\nu dx \tag{2.32}$$

The expressions for the fluorescence yields, F and F', still have many variables that have not been tabulated conveniently in literature. As a result, further simplifications will need to be made on the basis of reported experimental observations. These simplifications are outside the scope of this chapter and will be introduced in Chapter FIXME 4 along with the results of applying this model to various reactant mixtures.

19

CHAPTER 3

EXPERIMENTAL METHODS AND CONSIDERATIONS

The current chapter describes the facilities and apparatus used to study the flame characteristics in a Low Swirl Burner. The selection and implementation of diagnostic techniques used in this study are explained, as are data analysis methods used to process the acquired data.

3.1 LSB configurations

Two configurations of the Low Swirl Burner were tested for this study. There are referred to in what follows as Configurations A and B. Each configuration consists of the reactant flow inlet, the swirler device, the conduit to the combustion zone and the combustion zone itself. All swirlers tested for this work have an outer diameter, d_s of 38 mm (1.5 in). Other key dimensions of the swirlers tested are presented in Table 3.1.

Each configuration is housed in a high pressure testing facility. The testing facility consists of an air and fuel supply system, a pressure vessel with adequate optical access and an exhaust system for the products. Each testing facility is instrumented to measure temperatures and pressures which are then used to calculate various flow parameters of interest.

The design of the configurations tested, along with that of their respective test facilities are discussed in greater detail in this section.

Table 3.1: *The dimensions of the swirlers used and the respective perforated plates are presented. Each swirler is referred to by its vane angle (as in "$S_{37°}$").*

Geometric parameter	Swirlers		
	Configuration A		Configuration B
	$S_{37°}$	$S_{45°}$	$S_{40°}$
Swirler data			
Outer diameter, d_s, mm	38	38	38
Diameter ratio, $\frac{d_i}{d_s}$	0.66	0.66	0.66
Vane angle, α	37°	45°	40°
Theoretical Swirl Number, S	0.48	0.64	variable
Perforated plate data			N/A
Open area, mm^2	155.97	156.98	-
Blockage, %	71.54	71.36	-
Plate thickness, mm	1.27	1.27	-
Hole pattern	1 - 8 - 16	1 - 8 - 16	-
Hole location (dia), mm	0 - 10.2 - 19.1	0 - 10.2 - 19.1	-
Hole diameter, mm	2.79 - 2.79 - 2.84	2.82 - 2.82 - 2.83	-

3.1.1 Configuration A

Preliminary experiments involving velocity field mapping and flame imaging were performed using this configuration. The schematic of the high pressure test facility housing this configuration is shown in Figure 3.1, while the configuration itself is shown in greater detail in Figure 3.2.

3.1.1.1 Test Facility

Pressurized air is supplied from external tanks and heated in an indirect, gas-fired heat exchanger to about 500 K. The flowrate of the air is metered using a sub-critical orifice flow meter with a 38 mm (1.5 in) bore diameter Flow-Lin orifice plate capable of metering a maximum flow rate of 2.2 kg/s (1 lb/s). The orifice flow meter is instrumented with an Omega PX725A-1KGI pressure transmitter calibrated to a reduced pressure range of 0–2.758 MPa (0–400 psi), a shielded K-type thermocouple and an
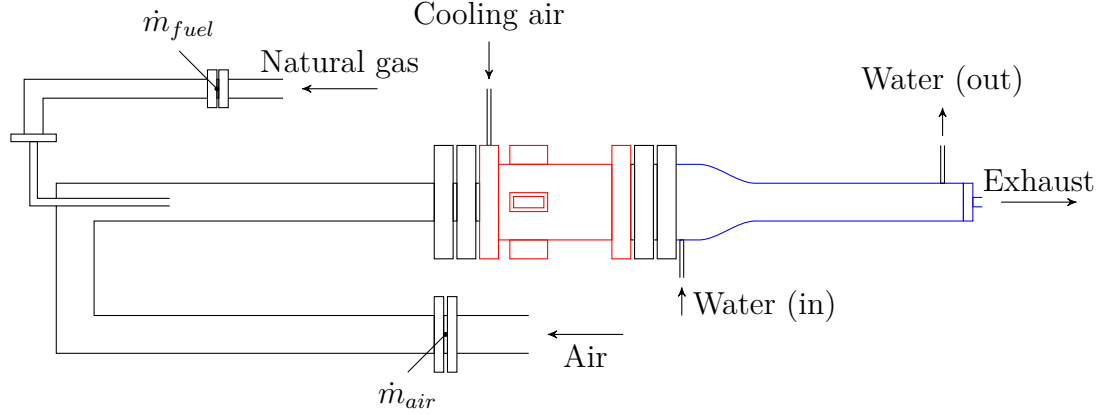
Figure 3.1: *A schematic of the high pressure testing facility where Configuration A was operated is shown. The pressure vessel is outlined in red, while the water-cooled exhaust section is outlined in blue. The locations of the orifice flow meters used to measure the mass flow rates of the preheated air and natural gas fuel are indicated.*

Omega PX771A-025GI differential pressure transmitter, calibrated to a reduced differential pressure range of 0–68.948 kPa (0–10 psid). The fuel (natural gas) is metered using a similar set up as the air line, with a sub-critical orifice flow meter. The fuel orifice plate is a Flow-Lin orifice plate with a bore diameter of 13.46 mm (0.53 in), capable of metering a maximum flow rate of 0.22 kg/s (0.1 lb/s). The upstream pressure is measured using an Omega PX725A-1KGI pressure transmitter (same as the air line) and the differential pressure is measured using a PX771A-100WDC differential pressure transmitter with a pressure range of 0–2.489 kPa (100 in H_2O). The temperature of the fuel is assumed to be the same as the nominal room temperature (300 K).

The air enters the inlet nozzle of the LSB through a 1.8 m (6 ft) long, 102 mm (4 in) diameter straight pipe section. The fuel flow is choked prior to mixing with the air flow at the head of the straight pipe section. The straight pipe section allows for the flow to be fully developed, and fully premixed before the reactants enter the burner. The combustor pressure and temperature are measured at the head of the inlet nozzle. The pressure is measured by an Omega PX181B-500G5V pressure transducer with a pressure range of 0–3.45 MPa (0–500 psi), while the temperature is measured using

a K-type thermocouple. 400

The pressure and temperature measurements are used to calculate the four primary flow parameters (combustor pressure, preheat temperature, reference velocity and equivalence ratio) for the LSB in real time. All measurements are monitored and recorded during the course of the experiment by a LabView VI. 404

The pressure vessel enclosing the combustor is designed to withstand pressures of up to 30 atm and is insulated from the combustor by a ceramic liner. Cooling for the pressure vessel and the quartz tube is provided by a flow of cold air introduced at the head of the pressure vessel. The cold air is drawn from the same external tanks as the main air line, but bypassing the heating system. The cold air flow is not metered, but its upstream pressure is coupled to the main air line so as to ensure a steady flow of cold air into the pressure vessel at all operating conditions. Optical access to the combustor is provided through four 25 mm (1 in) thick, 150 mm (6 in)×75 mm (3 in) quartz windows located 90° apart azimuthally. The view ports allow the combustor to be imaged from the dump plane to an axial distance of 150 mm (6 in) downstream. 414

The exhaust from the combustor is cooled by circulating cold water through a water jacket enclosing each section of the exhaust pipe. The length of the exhaust pipe sections is about 1.8 m (6 ft). The exhaust pipe section terminates in an orifice plug that provides back pressure to the combustion chamber. A different diameter orifice is used for each reference velocity condition tested. The exiting products are finally released to the building exhaust system. 420

3.1.1.2 Low Swirl Burner 421

The detail of the LSB configuration is shown in Figure 3.2. The premixed, preheated reactants reach the swirler through a converging nozzle that decreases linearly in diameter from from the inlet diameter of 102 mm (4 in) to the outer diameter of the swirler, 38 mm (1.5 in). At the swirler, the flow splits into two streams—one passing 425
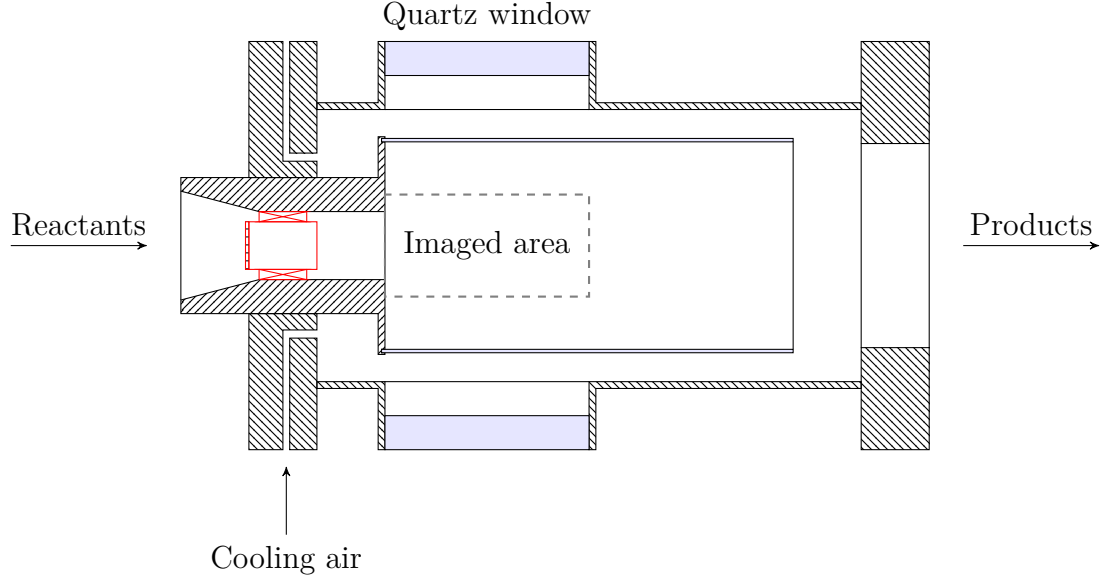
23

Figure 3.2: *A cross-sectional view of Configuration A in the pressure vessel is shown. The reactants enter from the left. The products mix with the cooling air and leave on the right. The location of the swirler in the inlet nozzle is highlighted in red. Also shown is the region of the combustion zone that can be imaged through the quartz windows.*

through the central section and another picking up swirl by flowing over the vanes in the annular region. The relative flow split between the two streams is controlled by inducing blockage into the central flow by means of a perforated plate. The swirler leads to a constant area nozzle, and is located one diameter upstream of an abrupt area change. At the area change, the reactants expand from the 38 mm (1.5 in) diameter nozzle into a 115 mm (4.5 in) diameter combustion zone. This expansion ratio is chosen so as to avoid confinement effects on the centerline flame flow field.[20]

The main combustion zone begins at the dump plane and is enclosed by a GE 214 quartz tube. The quartz tube is 300 mm (12 in) long and 115 mm (4.5 in) in diameter. The thickness of the quartz tube is 2.5 mm (0.1 in).

3.1.2 Configuration B

This configuration is used to image the flame structure of the LSB flame using CH PLIF. A schematic of the flow system of the test facility is shown in Figure 3.3, while

the LSB combustor itself is shown in greater detail in Figure 3.4.

3.1.2.1 Test Facility

This test facility shares the upstream supply of preheated air, cold air and fuel (natural gas) with the one used in Configuration A. The flow rate of the preheated air stream is measured using the same orifice flow meter system used in Configuration A—albeit with a smaller 12.921 mm (0.5087 in) diameter bore Flow-Lin orifice plate. The fuel system pressure is regulated from the building supply pressure to a lower required pressure by an adjustable TESCOM regulator and metered using a critical orifice flow meter. The critical orifice on the fuel line has a bore diameter of 0.8128 mm (0.032 in). The pressure upstream of the critical orifice is measured using an Omegadyne PX409-1.5KGI pressure transmitter with a range of 0–10.34 MPa (0–1500 psig) and the pressure downstream of the critical orifice is measured using a Dwyer 626 series pressure transmitter with a range of 0–3.45 MPa (0–500 psig). The downstream pressure can be used to verify if the critical orifice is choked during operation. The temperature of the fuel is measured upstream by a K-type thermocouple.

The air system is choked with a 5.41 mm (0.213 in) diameter critical orifice before mixing with the fuel. A short distance after mixing, the reactants are split into two separate streams for the central flow and the swirl flow. The central flow rate is measured using a 9.271 mm (0.365 in) diameter sub-critical orifice, instrumented with a Dwyer 626 series pressure transmitter with a range of 0–4.14 MPa (0–600 psig) for measuring the upstream pressure, a K-type thermocouple for measuring the upstream temperature and an Omega PX771-300WCDI differential pressure transducer with a range of 0–74.65 kPa (0–300 in H_2O). The swirl flow rate is measured similarly, using a 11.68 mm (0.46 in) diameter sub-critical orifice, a Dwyer 626 series pressure transmitter with a range of 0–5.52 MPa (0–800 psig), a K-type thermocouple and another Omega PX771A-300WCDI with a differential pressure range of 0–74.65 kPa

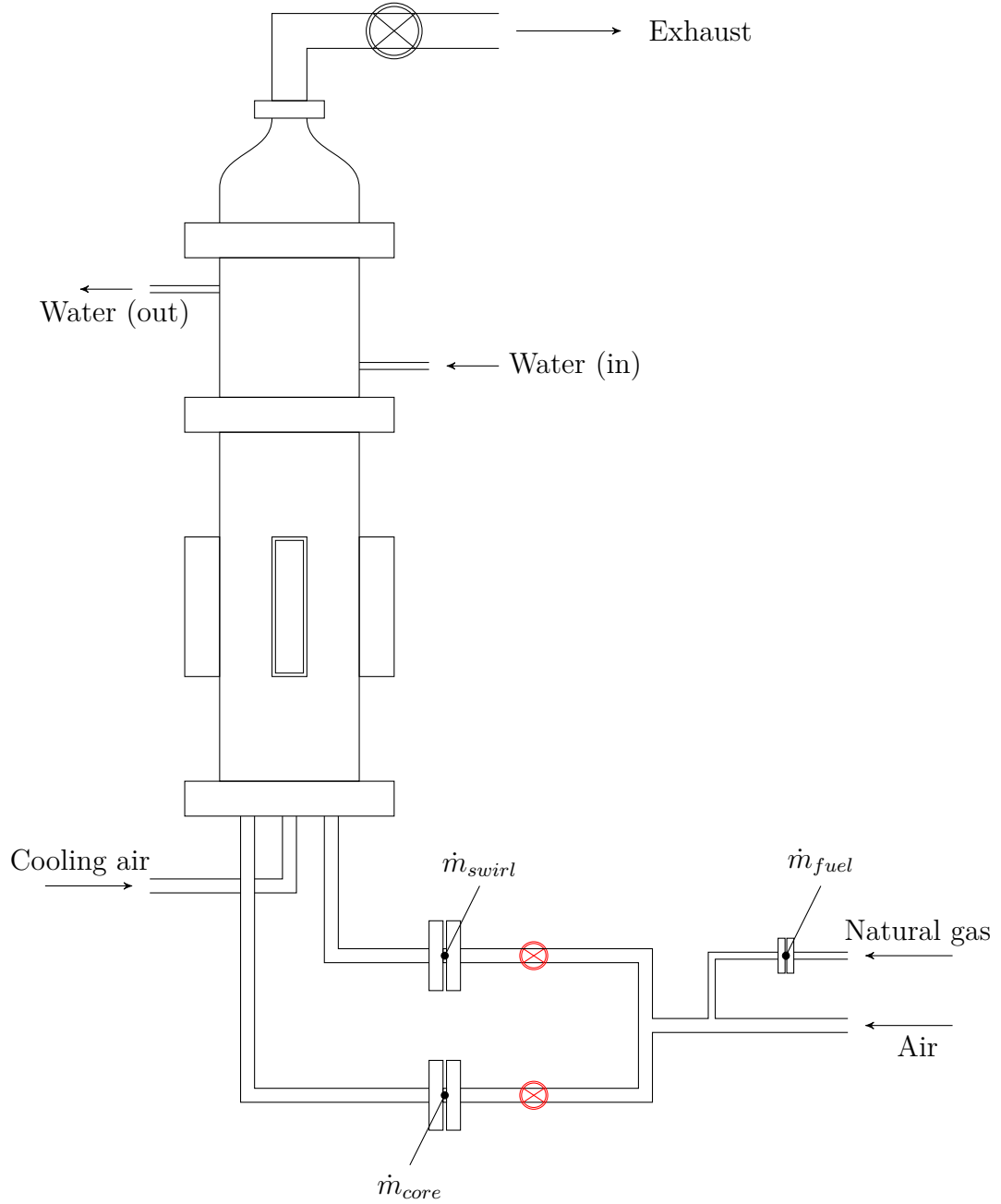Figure 3.3: *A schematic of the high pressure testing facility where Configuration B was operated is shown. The locations of the orifice flow meters on the reactant streams and fuel lines are shown. Valves (shown in* red*) on the swirl and core flow lines allow for the relative mass flow split to be varied between the two reactant streams. The upstream orifice flow meter on the preheated air line is not shown here.*

(0–300 in H$_2$O). The relative flow split between the two reactant streams is controlled by partially closing gate valves on the two lines.

The cooling air flow line is choked, but the flow rate is not metered. All measurements are monitored and recorded by a LabView VI.

The pressure vessel is rated for pressures in excess of 30 atm and is insulated from the combustor by a flow of cold air. The cold air enters the pressure vessel through two inlet ports and passes through a layer of steel ball bearings which renders the flow uniform spatially. The central and swirl flow reactant streams enter through separate ports and connect to the combustor. The pressure vessel has four viewports located 90° apart for optical access. Each viewport is covered by a 25 mm (1 in) thick, 178 mm (7 in) × 50 mm (2 in) quartz window. The LSB exit is located approximately halfway between the top and bottom edges of the window, allowing about 88.9 mm (3.5 in) of the combustion zone to be imaged through the window. Similar to Test Rig A, the exhaust section is cooled by circulating cold water through an enclosing water jacket. An adjustable gate valve on the exhaust line provides the back pressure necessary to pressurize the combustor. The products are vented into the same building exhaust system as Configuration A.

3.1.2.2 Low Swirl Burner

The design of this LSB configuration is presented in Figure 3.4. As described earlier, the reactants reach the LSB swirler device through two separate streams. The core/central stream passes through a plenum chamber which is filled with steel ball bearings before approaching the swirler through a smoothly contoured nozzle with a high contraction ratio. The annular/swirl stream reaches the swirler directly through a separate contoured nozzle. The contraction ratio is chosen to inhibit the formation of thick boundary layers in the reactant streams. The core stream passes through the central portion of the swirler, while the annular stream picks up swirl by passing

27

Imaged area

Cooling air   Core flow

Swirl flow

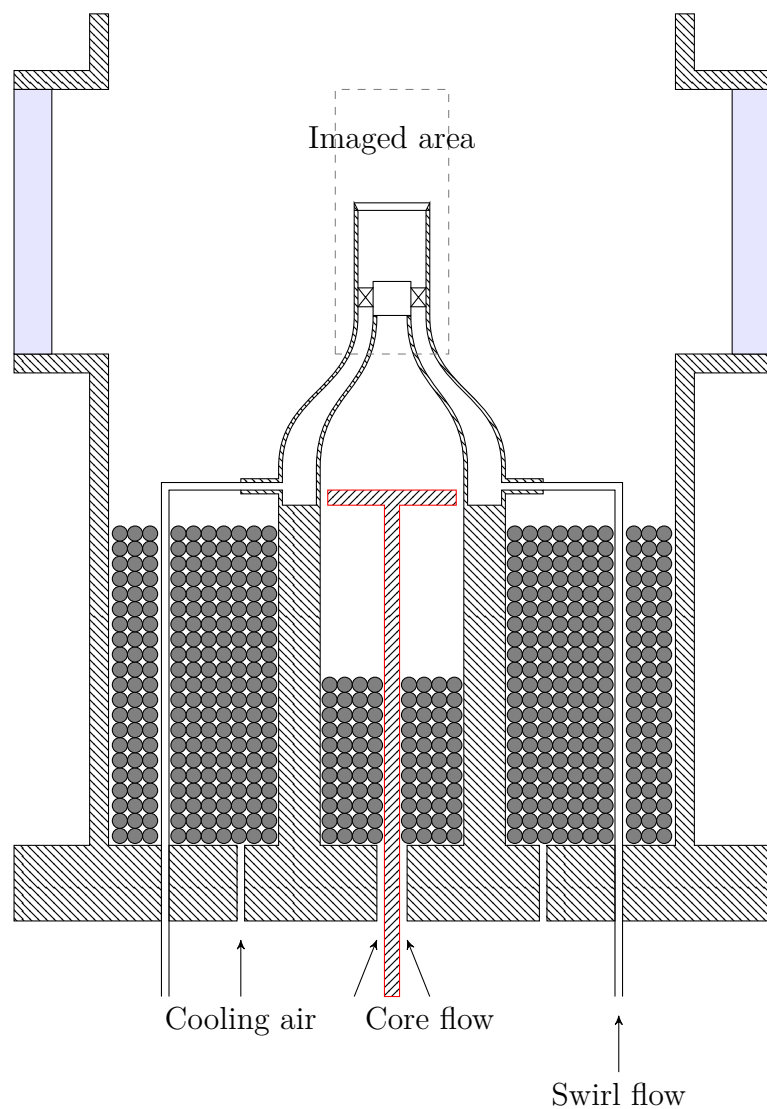Figure 3.4: *A cross-sectional view of Configuration B in the pressure vessel is shown. The reactants enter from below in two separate streams (core flow and swirl flow), along with cooling air. Stainless steel ball bearings inside the plenum chamber and outside make the core flow and the cooling air flow spatially uniform. The turbulence generator is located within the plenum and is outlined in* red.

through the vanes of the swirler. The swirler lacks a perforated plate covering the 491
central region as the primary function of the plate—regulating the relative mass flow 492
split—is performed by the test facility itself. 493

The swirler device is located at the beginning of a constant area nozzle which is 494
57.2 mm (2.25 in) in length. Following this, the reactants expand into the combustion 495
zone. 496

Unlike in Configuration A, there is no dump plane or quartz tube to provide 497
confinement to the combustion zone. The co-flow of cold air provides insulation to 498
the walls of the pressure vessel. Also, as mentioned earlier, the relative mass flow split 499
between the central and annular flows can be controlled directly. Finally, the level of 500
turbulence in the central flow can be adjusted by use of a turbulence generator[21] 501
located upstream in the plenum chamber. 502

3.2 Diagnostics 503

3.2.1 Laser Doppler Velocimetry 504

The velocity field of the LSB is mapped using a TSI 3-component LDV system. 505
Three wavelengths (514 nm, 488 nm and 476 nm) are separated from the output of a 506
5 W Argon ion laser by an FBL-3 multicolor beam generator. The individual beams 507
are split into two coherent beams which are then focused to intersect and produce 508
interference fringes within an ellipsoidal measurement volume with dimensions of the 509
order of 100 μm. For this purpose, two transceiver probes are mounted 90° apart 510
about the axis of the LSB. The setup is illustrated as a schematic in Figure 3.5. One 511
transceiver probe focuses the 514 nm and 488 nm beams in planes perpendicular to 512
each other, while the second probe focuses the 476 nm beams orthogonal to the other 513
two beams. Particles in the flow field crossing the interference fringes scatter the 514
laser light elastically and produce a sinusoidal signal whose frequency is proportional 515

29
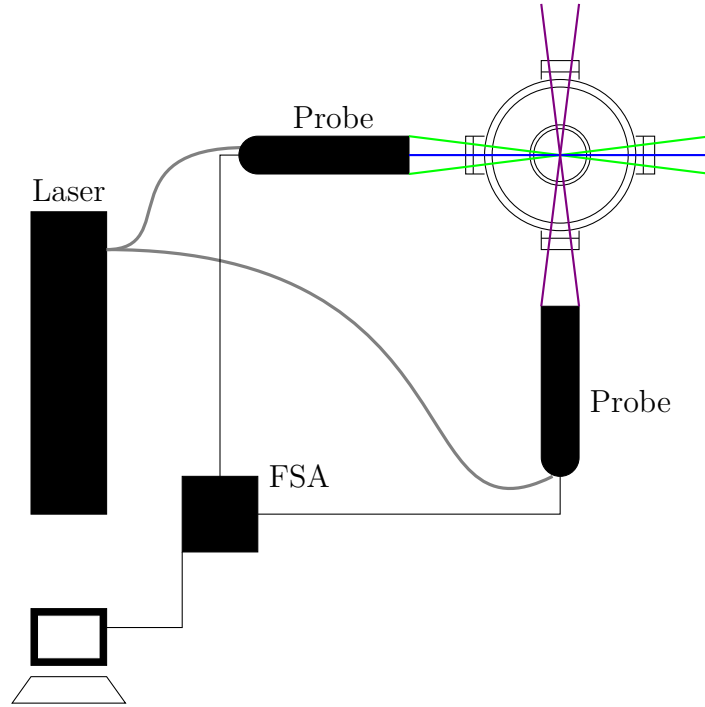
Figure 3.5: *The schematic shows the setup employed to map the velocity field of the LSB combustor using Laser Doppler Velocimetry. Three pairs of orthogonal beams are separated from the Argon Ion Laser output and conveyed by fiber optic cables (gray) to optical probes mounted 90° apart about the axis of the LSB combustor. The green, blue, and violet beams in the schematic represent the 514 nm, 488 nm and 476 nm wavelengths. The signal is collected by the transceiver probes and analyzed by the FSA module. The results are saved for further analysis.*

to the velocity of the particle. The transceiver probes collect this scattered light and each wavelength is detected separately by a PDM-1000-3 three-channel photodetector module. The output from the photodetector is processed by an FSA-3500-3 signal processor. The resulting three components of the particle/flow velocity are recorded by the FlowSizer software.

Since the concentration of particulate matter (primarily dust particles) in the airflow is very low, the flow needs to be artificially seeded to facilitate LDV measurements in a reasonable amount of time. The choice of seeding particles to be used and their mean diameter are decided by the characteristics of the flow to be imaged.[22] Since the LSB flow field is a reacting one, the particles need to have high melting points. Further, the particles need to be small enough to follow the flow closely and large enough or reflective enough to scatter light efficiently in the measurement volume. Based on these requirements, commercially available alumina particles with a mean particle diameter of 5 μm were chosen for this study. In order to uniformly seed the flow, a novel seeding generator was designed as described in Appendix A. The seeding particles were introduced slightly upstream of the 1.8 m (6 ft) long straight pipe section in Test Rig A.

LDV data is only acquired at atmospheric pressure conditions. At high pressure conditions, the reacting LSB flow field produces sharp refractive index gradients that rapidly shift in the turbulent flow field. This causes strong beam steering effects making it very difficult for the laser beams to reliably intersect within such a small measurement volume. The long distance traveled by the beams in the test rig further exacerbate this problem, making LDV data nearly impossible to acquire at such conditions.
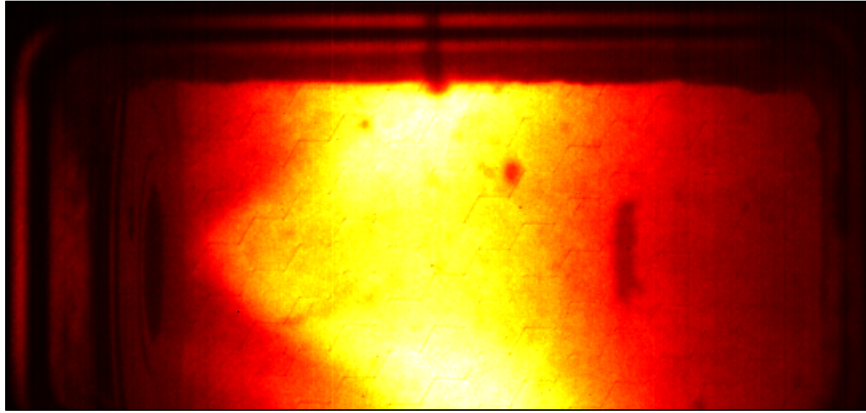
3.2.2 CH* chemiluminescence

The LSB flame is imaged using one of two 16-bit intensified CCD cameras—PI Acton
1024×256 or 512×512 pixels—with a 28 mm f/2.8 camera lens. CH* chemilumines-
cence is filtered using a bandpass filter centered on 430 nm with a FWHM of 10 nm.
At each operating condition, 100 instantaneous images are acquired with an exposure
of 1 ms. An additional 100 instantaneous images are acquired with no flame and
averaged to yield the background for correcting the flame images.

CH* chemiluminescence has several advantages over flame chemiluminescence
from other radicals such as OH*, C_2*, etc. First, the CH* emission occurs around 430
nm and is less affected by blackbody radiation from the walls of the combustor com-
pared to longer wavelength detection, e.g., C_2*, which emits around 514 nm. Second,
the intensity of the chemiluminescence from CH* is known to scale well with heat
release in the combustor[23], unlike C_2*. Third, the emitted light can be gathered
with high quantum efficiency by the intensified CCD cameras available for this study.
Particularly, the quantum efficiency of the 18 mm Gen III HB filmless intensifier used
by the 512×512 camera is about 45% at 430 nm, compared to about 10% at 310 nm,
where OH* chemiluminescence peaks.

3.2.2.1 Image Processing

The flame chemiluminescence images acquired are background-corrected and aver-
aged. The resulting mean is the line-of-sight integrated, time-averaged image of the
flame. Strictly speaking, this is not the same as a real average obtained from a long
exposure image as the instantaneous images are obtained through a periodic sam-
pling process and hence, are prone to statistical errors. However, the behaviour of
the flame can be assumed to be sufficiently random that the mean obtained is ad-
equately representative of the true average. Figure 3.6a shows a typical mean CH*
chemiluminescence image prepared in this manner.

(a) *Average CH* chemiluminescence image*
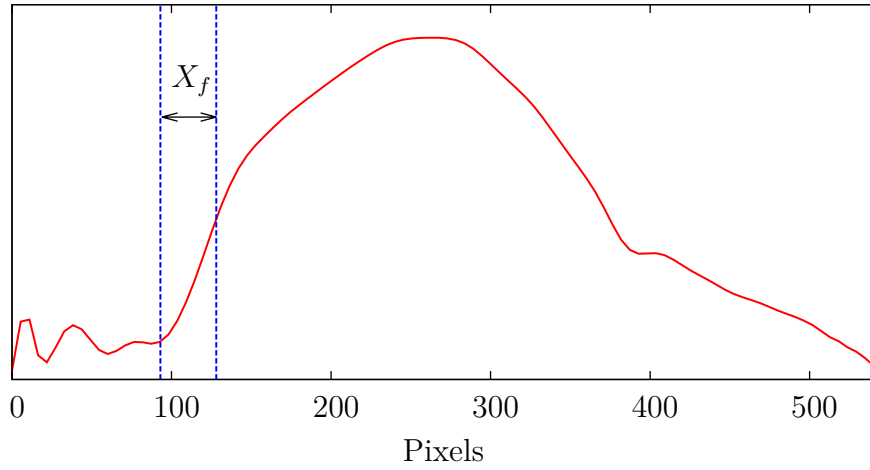
(b) *Centerline CH* chemiluminescence intensity*
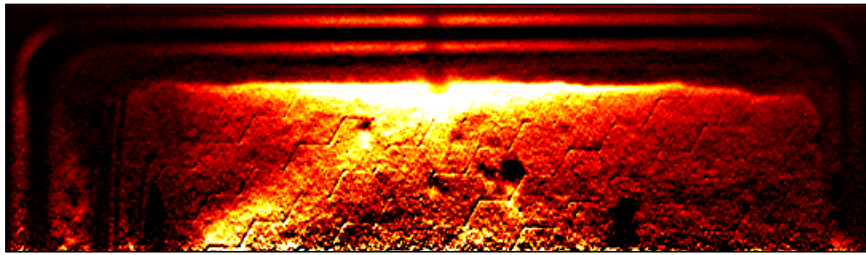
(c) *Abel deconvoluted half-image*

Figure 3.6: *These images illustrate the processing of a typical CH* chemiluminescence dataset. The top image is the mean of 100 frames and shows the LSB flame at 9 atm. The flame standoff distance is calculated by locating the inflection point in the smoothed intensity profile (middle). An Abel deconvolution (bottom) can be used to highlight the flame brush and measure the angle of the flame.*

Even when background-corrected, the walls of the combustor are not at zero in- ₅₆₆
tensity in the average chemiluminescence image. This is particularly noticeable near ₅₆₇
the dump plane where there is no flame present and yet the walls are clearly illumi- ₅₆₈
nated. The source of this background illumination is mostly the chemiluminescence ₅₆₉
from the flame scattering off the combustor and pressure vessel walls. The contribu- ₅₇₀
tion from blackbody radiation from the heated walls is less significant in the narrow ₅₇₁
wavelength range imaged. This is evident from images acquired immediately after a ₅₇₂
flame blowout which show the walls to be nearly dark. ₅₇₃

The averaged chemiluminescence image allows us to measure the flame stand- ₅₇₄
off distance by following the intensity profile along the centerline of the combustor. ₅₇₅
The intensity profile rises sharply when passing the flame standoff location. Thus, ₅₇₆
the flame standoff location can be ascertained by finding the inflection point in the ₅₇₇
intensity profile. ₅₇₈

The profile of the average chemiluminescence intensity along the centerline of the ₅₇₉
sample case from Figure 3.6a is shown in Figure 3.6b, showing the flame standoff ₅₈₀
distance. The distance from the dump plane, measured in number of pixels on the ₅₈₁
image and scaled by the appropriate magnification factor yields the flame standoff ₅₈₂
distance, X_f. The determination of the flame standoff location by this method pro- ₅₈₃
vides a suitable and deterministic means to locating the leading edge of the flame ₅₈₄
front. ₅₈₅

The average image can be processed further to yield more spatially resolved in- ₅₈₆
formation about the flame brush. Under the reasonable assumption that the average ₅₈₇
LSB flame is axially symmetric about the centerline of the combustor, a tomographic ₅₈₈
deconvolution technique called an Abel deconvolution[24] can be used to convert the ₅₈₉
line-of-sight integrated image to a radial map of chemiluminescence intensity. In ₅₉₀
effect, this shows the shape and structure of the average flame brush. The Abel ₅₉₁
deconvolution of the sample data from Figure 3.6a is shown in Figure 3.6c. ₅₉₂
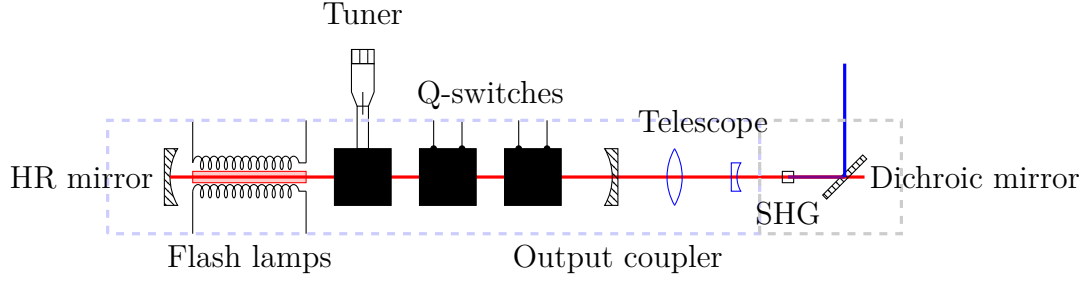
34

Figure 3.7: *A schematic of the components of the PAL 101 Alexandrite laser is shown. The resonator formed by a High Reflection (HR) mirror and an output coupler is built around an alexandrite rod (red) pumped by flashlamps. The frequency of the output is selected by a tuner mechanism. Only one of the two Q-switches was used for this study. The laser beam is reduced in diameter by a collimating telescope (blue) before passing through the Second Harmonic Generator (SHG). The UV beam is separated from the fundamental by a dichroic mirror and exits the laser. The fundamental beam terminates within the laser in a beam dump.*

The Abel-deconvoluted image provides an relatively easy means to determining the angle of the flame brush. A straight line joining two points located at the center of the flame brush intersects the axis of the combustor at this angle. The angle of the flame is denoted by θ_f.

Using the Abel deconvolution to study the flame brush suffers from two main drawbacks. First, the system of equations describing the Abel deconvolution is only valid as long as the entirety of the flame is visible. This is only satisfied in the initial region of the LSB where the diameter of the flame brush is smaller than the height of the optical viewport. At further downstream locations, the flame is not imaged in its entirety. This causes the spurious bright regions near the top of the window in Figure 3.6c. The second limitation of the Abel deconvolution technique stems from the high incidence of errors along the centerline (where $r \to 0$). Due to this, any study of the flame brush thickness at the flame stabilization point—a metric of considerable importance—is all but impossible using this tomographic technique.

3.2.3 CH Planar Laser-Induced Fluorescence

The CH PLIF setup uses the frequency-doubled output of a Light Age PAL 101 alexandrite laser tuned to $\lambda \approx 387.2$ nm. The design of the laser is shown schematically in Figure 3.7. The active medium is a 150 mm (6 in) long, 5 mm (0.197 in) diameter alexandrite rod. The rod is placed between two flashlamps within the resonator cavity formed by two spherical mirrors. A birefringent tuning mechanism is placed within the resonator to allow the user to select the frequency of the output beam. The tuning mechanism is coupled to a micrometer whose reading relates linearly to the output wavelength. The tuning mechanism allows the fundamental wavelength to be varied between 720–780 nm, with peak gain at about 755 nm. The resonator cavity also contains two Q-switches, which allow the laser to optionally operate in double-pulsed mode. For this study, however, only one Q-switch is used and the laser is operated in single-pulsed mode only.

The diameter of the fundamental beam exiting the output coupler is reduced by a collimating telescope. This is done in order to increase the efficiency of conversion of the frequency-doubling crystal. The second harmonic portion of the beam is separated from the fundamental by a dichroic mirror and exits the laser. The fundamental beam is terminated at a beam dump within the laser. The exit beam diameter is about 1 mm.

The alexandrite laser is capable of operating at frequencies of up to 15 Hz. Laser power is controlled primarily by varying the voltage applied to the flash lamps. When operating with a high flash lamp voltage, it is recommended that the frequency of pulsing be reduced to allow more time to dissipate the heat build up within the alexandrite rod. All experiments conducted as part of this study operated the laser at 10.0 Hz.

The typical power output of the laser is about 15 mJ/pulse. The pulsewidth of the laser is about 60-80 ns and is observed to decrease with increasing flash lamp

voltage. The linewidth of the fundamental beam is determined by the manufacturer to be 150 GHz at $\lambda = 775$ nm. Assuming the spectral profile of the laser to be a Gaussian, the linewidth of the frequency-doubled beam can be determined. The Full Width at Half Max (FWHM) of a Gaussian curve scales linearly with the standard deviation of the curve. When convoluted with itself, the new standard deviation is $\sqrt{\sigma^2 + \sigma^2}$ or $\sqrt{2}$ times that of the original curve. Thus, the new linewidth is $150 \times \sqrt{2}$ = 212 GHz or 7.07 cm^{-1}. In wavelengths, this represents a spread of about 1.06 Å.

3.2.3.1 Imaging system

All LIF imaging is performed with an intensified PI Acton 512×512 camera. The intensified camera is equipped with an 18 mm Gen III HB filmless intensifier with a quantum efficiency of about 45% in the 420–440 nm range. The lens is chosen depending on imaging requirements of each experiment. In all cases, elastic scattering from the laser beam is attenuated by a 3 mm thick GG 420 Schott Glass filter.

3.2.3.2 Laminar Flame setup

Preliminary experiments to evaluate the CH PLIF technique are performed on a laminar flame. The choice of a laminar flame as the subject allows us to neglect effects of strain and turbulence on the flame. Further, laminar flames are more readily simulated by reaction kinetics packages like Chemkin with high fidelity.

These experiments are conducted on an laminar, methane-air flame stabilized on an unpiloted Bunsen burner with an inner diameter of 10.16 mm (0.4 in). The air flow rate is measured and regulated using a Dwyer rotameter with a range of 0–20 SCFH calibrated using a Ritter drum-type gas meter. The natural gas flow rate is metered using a Matheson FM 1050 602 rotameter with a range from 0–1230 SCCM. This flowmeter is calibrated using a Sensidyne Gilibrator 2 bubble flow meter system.
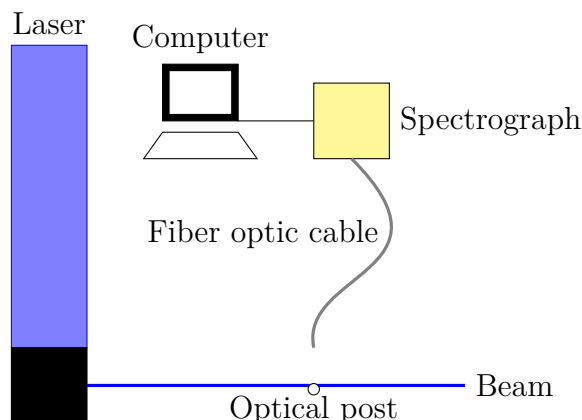
Figure 3.8: *The figure above shows the schematic of the experiment performed to calibrate the wavelength of the laser output. The laser output (containing mostly UV, but also a small portion of the fundamental frequency) is glanced off a steel optical post. The scattered light is gathered by a fiber optic cable (gray) and sent to a spectrometer. The spectrum is analyzed to track the location of the fundamental frequency with tuner position. The UV peak is not tracked as the spectrometer is not calibrated for that wavelength.*

3.2.3.3 Laser Wavelength Calibration

As described earlier, the output wavelength of the PAL 101 alexandrite laser is controlled using a micrometer-coupled birefringent tuning mechanism. The wavelength of the laser beam varies linearly with the micrometer reading. Initially, the manufacturer-supplied calibration for the micrometer was found to be inaccurate. This required an experiment to calibrate the laser output wavelength against the micrometer reading in order to determine the slope and offset of the calibration curve accurately.

A schematic of this experiment is shown in Figure 3.8. The laser beam is glanced off a steel optical post and the scattered light is collected using a fiber-optic cable coupled to an Ocean Optics HR 2000 spectrometer. The spectrometer is pre-calibrated using 50 wavelengths in the 400–850 nm range from the output of a Neon discharge lamp source. The spectrometer is also intensity corrected over this range using a black body source. The estimated error in the resolution of the device is about 0.1 nm (1 Å).
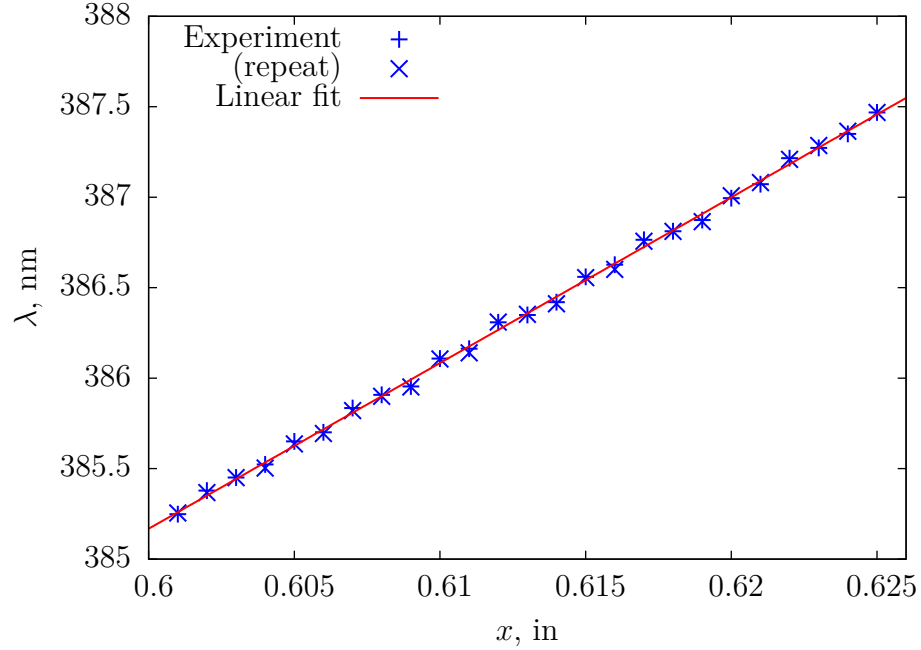
38

Figure 3.9: *The wavelength of the second harmonic beam of the laser is plotted above against the tuner position(x). The data shows excellent repeatability and falls on a linear trend. The equation for the linear curve fit is $\lambda = 330.213 + 91.5908x$, where the units of λ and x are nm and in, respectively.*

The laser micrometer is traversed from 0.600 in to 0.625 in in steps of 0.001 in. The experiment is repeated by traversing the micrometer from 0.625 in back to 0.600 in along the same points to ensure repeatability and estimate the variation due to hysteresis. The calibration is performed using at the fundamental wavelength of the laser as the second harmonic wavelength falls outside the spectrometer's range. Each spectrum recorded is integrated over 512 ms and averaged over 10 such acquisitions. The background-corrected peak of the spectrum is then modeled as a Gaussian and the location of the center of the Gaussian waveform is recorded.

The results from this experiment are shown in Figure 3.9. The plot demonstrates that the variation of the second harmonic wavelength (obtained by halving the fundamental wavelength) with the position of the tuner micrometer is linear. Further, there is little difference between the measurements taken while increasing and decreasing the micrometer position. This indicates that any effects of hysteresis in the

micrometer position are minimal. The calibration equation relating the micrometer 686

position to the output wavelength is obtained by applying a linear curve fit to the 687

data points on the graph as shown in Figure 3.9. 688

CHAPTER 4

CH PLIF SIGNAL MODELING AND VALIDATION

4.1 CH PLIF Development/Preliminary Experiments

The CH PLIF imaging system was evaluated for use in imaging hydrocarbon flames by performing two preliminary experiments. First, an excitation scan was performed to locate the optimal wavelength to excite the CH radicals in a typical hydrocarbon flame. The variation in this optimal wavelength with temperature and pressure was calculated and found to be within acceptable bounds. Second, a test of the linearity of the LIF signal with respect to the incident laser intensity was performed. The setup and results of these experiments are described in the following subsections.

4.1.1 Excitation scan

An excitation scan is performed by tuning the output of the alexandrite laser from λ = 387.077 nm to 387.260 nm. This serves two purposes. First, it locates the optimal wavelength to excite the CH radicals that results in the highest fluorescence yield. Second, the variation of the signal intensity can be compared with simulated profiles from LIFBASE or other spectroscopic calculations and our estimation of the laser linewidth can be validated. Knowing the laser linewidth accurately is important for modeling the LIF signal. This aspect will be discussed in further detail later in this thesis/chapter FIXME.

A schematic of the excitation scan experiment is shown in Figure FIXME. The intensified PI Acton 512×512 camera described in Section 3.2.2 is used to image a premixed, laminar methane-air flame operating at close to stoichiometric conditions. The laminar flame is stabilized on the Bunsen burner described in Section 3.2.3.2. The

alexandrite laser is operated at a power of 16 mJ/pulse in the second harmonic. The 712

sheet forming optics consist of a +50 mm cylindrical lens and a +250 mm spherical 713

lens placed 300 mm apart. The optics form the beam into a collimated sheet about 714

25 mm (1 in) tall, focused to a thickness on the order of 100 μm at the flame location. 715

The sheet passes through the center of the flame and the edges of the sheet are blocked 716

by razor blades to prevent reflections from the burner from saturating the camera. 717

The induced fluorescence in the flame sheet is imaged perpendicularly by the 718

intensified camera using an 85 mm f/1.8 Nikon AF Nikkor lens. This gives a magnifi- 719

cation of approximately 62 μm/pixel. The camera is triggered by the flash lamp sync 720

signal from the laser system and the intensifier is gated over 300 ns, encompassing the 721

70 ns laser pulse. The long gate width gives the intensifier enough time to prepare to 722

receive the fluorescence, preventing signal loss due to irising. The gate width is still 723

short enough that minimal flame chemiluminescence or ambient lighting is recorded 724

in the images. 100 instantaneous images are acquired for each excitation wavelength 725

to acquire a good estimate of the mean fluorescence signal, μ_{sig}. 726

Figure FIXME shows a sample CH PLIF image from this dataset. The images 727

are background-corrected by subtracting the laser scattering (recorded without the 728

flame). The fluorescence signal is calculated from these images using three alternate 729

approaches. 730

In Method I, two "windows" are identified that include the straight sections of the 731

laminar flame. The average fluorescence signal in each frame is calculated by taking 732

the average of all the emitting pixels in the two windows. A pixel is designated as an 733

emitting pixel if its intensity exceeds the standard deviation of a typical background 734

pixel by at least a factor of five. The average of this value over all the frames is 735

designated as the mean fluorescence signal, μ_{sig}. In Method II, the intensity of the 736

pixels is integrated over a straight line connecting the inner and outer edges of the 737

flame. The straight line is chosen along the beam so that the beam intensity does 738

not vary along the integration path. The integration is performed on the left and 739
right arms of the flame, giving two readings per frame. The mean of these values over 740
all the frames is recorded as the mean fluorescence signal, μ_{sig}. In Method III, the 741
midpoints of the straight lines from Method II are located and the average of their 742
intensities, over all the frames is recorded as the mean fluorescence signal, μ_{sig}. The 743
regions of interest for each of these methods is highlighted in Figure FIXME. 744

The result of this investigation is shown in Figure FIXME. The calculated mean 745
fluorescence signals from the three methods are plotted against a LIFBASE simulation 746
of the absorption spectrum of the CH $B-X$ transition. The profiles are appropriately 747
scaled to match the LIFBASE simulation at the maximum value and at the minimum 748
value. The LIFBASE simulation is performed for a thermalized system at 1800 K, at 749
atmospheric pressure. Further, the instrument linewidth is specified to be the same 750
as our estimate of the laser linewidth (1.06 Å). 751

The profiles of the calculated and scaled mean fluorescence signals are observed to 752
agree extremely well with the LIFBASE simulation result. The discrepancies between 753
the three methods is minimal. 754

The results indicate that the optimal excitation wavelength, corresponding to the 755
highest mean fluorescence signal, is about 387.2 nm. For the rest of the experiments 756
performed in this work, the laser is operated at this wavelength. The results also 757
help verify that the calibration of the micrometer is accurate and the wavelengths are 758
precisely adjustable. Finally, the results validate that our estimated laser linewith, 759
1.06 Å, is accurate. This value can now be used in subsequent calculations of the LIF 760
signal levels. 761

4.1.2 Linearity test 762

As explained in Chapter FIXME, the variation of the fluorescence signal with the 763
excitation laser intensity exhibits a saturation curve. In the weak excitation limit, 764

43

the variation is linear and scales with the energy input. For reasons explained in 765
Chapter FIXME, it is preferred to operate in this linear regime. 766

An experiment is performed to verify the linearity of the system response at the 767
intensities at which the flames are imaged for this work. The schematic of the setup is 768
shown in Figure FIXME. The laser is tuned to the optimal wavelength as determined 769
in Section 4.1.1, and operated at 10 Hz. The frequency-doubled beam is directed at a 770
steady, laminar, methane-air Bunsen flame operating at a slightly rich stoichiometry. 771
The edges of the beam are clipped by an aperture to produce a sharp edge and to 772
avoid unnecessary reflections from the burner. No optics are used to refract the beam 773
in any way. 774

The flame is imaged by the PI Acton 512×512 intensified camera equipped with a 775
50 mm, f/1.8 AF Nikkor lens. Elastic scattering is attenuated by a 3 mm thick GG 420 776
Schott glass filter. The magnification achieved by this set up is about 44 μm/pixel. 777
The LIF signal from the flame is recorded in 300 ns gates and accumulated 150 times 778
before being read out. For each case, a corresponding laser scattering image is also 779
recorded for estimating the background. The flame chemiluminescence and ambient 780
background are also recorded for the same purpose. 781

For this experiment, varying the intensity of the laser beam by changing the flash 782
lamp voltage or even the Q-switch timing is not preferred as either would alter the 783
pulse width of the beam. Instead, quartz disks and blocks of varying thickness are 784
introduced into the beam to produce an intensity loss, while preserving all other char- 785
acteristics of the beam. The quartz elements decrease the intensity of the laser beam 786
through reflection, scattering and absorption. The stray reflections and scattering 787
from the quartz elements are contained by enclosing the elements in a box and pre- 788
venting these from being recorded by the camera. In this manner, the laser power is 789
varied from 10 mJ/pulse to 0.5 mJ/pulse and back. 790

The acquired images are background-corrected and the intensity is conditionally 791

averaged over pixels with a non-zero intensity in the region where the fluorescence 792
occurs. The average fluorescence intensity values thus obtained are plotted against 793
the corresponding laser intensity and shown in Figure FIXME. A sample image high- 794
lighting the region of interest is also shown alongside. 795

The LIF signal is observed to increase monotonically with increasing laser inten- 796
sity. At the lower intensities, the variation is very nearly linear, with marginal scatter 797
and only one significant outlier. At intensities above 1 J/cm^2 however, there is sig- 798
nificant scatter in the data and the linear trend obtained from the low intensity cases 799
cannot be reliably extended over this region. 800

The results indicate that as long as the intensity of the laser sheet is kept below 801
1 J/cm^2, the assumption of operating in the linear regime is valid. 802

4.2 Fluorescence Signal Modeling 803

In Chapter FIXME 2, we derived the expression for the LIF signal as a function of 804
the thermodynamic conditions and the local composition. The expression requires 805
the pre-knowledge(?) of several spectroscopic constants of the CH system. 806

As described in Chapter FIXME 2, the excitation scheme used in this study pro- 807
duces fluorescence through a three-step process. First, the CH radicals in the ground 808
state $X^2\Pi, v = 0$ are excited by the incident radiation to the second electronically 809
excited state $B^2\Sigma^-, v = 0$. This excitation occurs near the R-bandhead and targets 810
the ground state CH radicals present in the rotational energy levels, $N = 5$ through 811
9. The upper electronic state $B^2\Sigma^-, v = 0$ is nearly degenerate with the $A^2\Delta, v = 1$ 812
energy level. This leads to the population of the $A^2\Delta, v = 0, 1$ energy levels due to 813
collisional energy transfer. The resulting fluorescence collected is primarily the result 814
of three spontaneous transitions — $A \to X(1, 1)$, $A \to X(0, 0)$ and $B \to X(0, 1)$. 815
These transitions are shown in Figure FIXME. 816

The primary goal of this exercise of modeling the CH fluorescence signal intensity 817

45

is to gage the feasibility of using CH PLIF to study various premixed flames, rather than to quantitatively calculate the amount of CH present in the flames. As such, we are more interested in the order of magnitude of the PLIF signal, rather than the absolute value of it.

The intensity of the CH fluorescence signal may be written as a function of the amount of CH radicals present in the excited state and the probability of spontaneous emission from said state.

In Equation 2.22, S is the total number of photons emitted per unit time, n is the number of excited CH radicals in a unit volume, V is the volume from which the signal is observed. The Einstein coefficient for spontaneous emission, A represents the probability of spontaneous emission between the two involved energy states. The predicted signal intensity represents the total number of photons emitted in all directions. In reality, only a fraction of these emitted photons will be recorded by the collection system. This fraction is a function of the experimental setup and depends on the collection angle, the efficiency of the optics and the detector used to record the signal. This fraction is left out because our objective is only to predict the relative variation in the signal between various premixed flames.

This formulation of the signal intensity implicitly makes the following assumptions.

1. The fluorescence emission is predicted at steady state.

2. The collection volume is optically thin and an emitted photon is not reabsorbed within the flame itself. This is a reasonable assumption to make, since the flame thickness and the thickness of the laser sheet are both typically quite small.

As described earlier, an accurate model of the CH system should involve five energy levels — $X(0)$, $B(0)$, $A(1)$, $A(0)$, and $X(1)$[1]. Such a model would also have to account for collisional transfers between each of these levels, in addition to spontaneous

---

[1] In this notation, the letter represents the electronic energy level and the number in the parentheses represents the vibrational quantum number of the energy level

and stimulated transitions. The mathematical solution quickly becomes complicated $_{843}$ and tedious. Further, it would involve several rate coefficients that have not been $_{844}$ measured in experiments done so far. $_{845}$

4.3 Results $_{846}$

Comparison of CH concentration predicted by GRI Mech and San Diego mechanisms $_{847}$ for methane. $_{848}$

CHAPTER 5

LSB FLAME CHARACTERISTICS

In Chapter FIXME 2, we introduced the salient features of the Low Swirl Burner (LSB) flow field and discussed the mechanisms by which the LSB flame is stabilized. Further, various characteristics of the LSB flame that can be measured from flame images were outlined. To recapitulate, these are the flame location, flame shape and the flame structure. The first two are quantified by the flame standoff distance, X_f, and the flame angle, θ_f, respectively.

In the same chapter, we introduced the four flow parameters that describe an op- erating condition for the LSB — the combustor pressure, p, the preheat temperature, T, the mass-averaged inlet velocity (also called the reference velocity, U_0), and the equivalence ratio of the premixed reactants, ϕ. We further introduced a geometric parameter — the angle of the vanes of the swirler, α, which affects the amount of swirl present in the flow field.

The LSB flame was studied over a range of operating conditions, and the effect of flow and geometric parameters on the reacting flow field were investigated. The results of these investigations are presented in this chapter.

5.1 Effect of reference velocity

In typical gas turbine applications, varying the loading on the engine does not affect the reference velocity. However, since the reference velocity is a design parameter, the effect it has on the flame characteristics has implications for the design of future LSB-based gas turbine engines.

One of the key objectives of this thesis is to investigate how the LSB flame stabi-

lization operates at high pressure conditions. The simple model described in Chapter FIXME 2 predicts a self-similar flow field for the LSB at all reference velocities. This implies that the reference velocity will have no discernible impact on the flame stand-off distance. This result is desirable for gas turbine designers, since the flame location and shape can be assumed to be constant. Limited testing conducted in published works confirmed this behavior at atmospheric pressure conditions with no preheat.

In order to verify the validity of this model at high pressure conditions in the presence of substantial preheat, the LSB was operated at a pressure of 6 atm over a range of reference velocities from 10 m/s to 40 m/s. For these tests, the $S_{37°}$ swirler was used. In a parallel series of tests, the $S_{45°}$ swirler was tested at a pressure of 3 atm at a reference velocities of 40 and 80 m/s. The location of the flame was measured from CH* chemiluminescence images, and the results are presented in Figure FIXME.

There is essentially no systematic variation in the flame standoff distance or the flame angle for the low velocity, $S_{37°}$ tests. Based on the model, this can be interpreted as the increase in reference velocity producing a concomitant increase in the turbulent flame speed at the flame stabilization location, negating any change in the flame's location. In other words, the flow field appears to retain its self-similarity, even at elevated pressures and temperatures.

When the $S_{45°}$ swirler was tested at higher reference velocities, however, the flame location shifted downstream sharply. This indicates potential limitations to the simple flame stabilization model that may not predict the behavior of the LSB flame at elevated pressures and temperatures, particularly at high reference velocities.

A possibe cause of this limitation can be explored by considering the effect of increased reference velocity on the turbulent combustion regime in which the LSB combustor operates. Previous studies have primarily operated the LSB in the flamelet regime where the modified Damköhler model predicts the behavior of the turbulent flame speed with reasonable fidelity. At elevated pressures, both the laminar flame

49

speed of the reactants, S_L and the flame thickness, δ_f are diminished. This places the operating regime higher and more to the right on a Borghi diagram, as shown in Figure FIXME. While increasing the reference velocity did not affect the turbulent combustion regime at lower pressures in a flamelet combustion regime, at elevated pressures the flame may be transitioning into the thin reaction zone regime. This transition would cause a reduction in S_T/S_L, or at least a lesser increase, and the turbulent flame speed would no longer be expected to increase in step with U_0 and the increased levels of turbulence. This would explain the the observed downstream shift of the high pressure LSB flame at high reference velocities.

5.2 Effect of preheat temperature

The preheat temperature of the reactants is a key flow parameter, especially for gas turbine combustors. In general, the rates of most chemical reactions in the flame zone are highly sensitive to the temperature of the reactants. For the LSB in particular, the temperature of the incoming flow directly affects its viscosity and consequently, the velocity field in the flame stabilization region. Thus, studying the effect of the preheat temperature on the LSB flame and flow field is important.

In order to explore this in greater detail, the velocity field of the combustor was mapped using Laser Doppler Velocimetry (LDV). The conditions were chosen to study the effect of increasing the preheat temperature on both reacting and non-reacting LSB flow fields. Further, the study includes both low and high reference velocity cases. The relevant flow parameters relating to these tests are presented in Table FIXME. All LDV tests were limited to atmospheric pressure conditions. Implementing the LDV technique at elevated pressures proved difficult due to beam steering issues, coupled with impractical turn-around times between the successive runs that would be required to obtain sufficent LDV data points for analysis.

The normalized centerline mean and rms axial velocity profiles for the three cases

are presented in Figure FIXME. The abscissa represents the distance from a point ^{925} called the virtual origin, X_0. The virtual origin is defined as the imaginary location ^{926} where the extrapolated linear axial velocity profile reaches the reference velocity in ^{927} magnitude. The extrapolation is indicated in Figure FIXME by a dashed line. ^{928}

As noted in Chapter FIXME 2, previous studies[25] reported that mean axial ^{929} stretch — the normalized slope of the linear decay of axial velocity — at the inlet of ^{930} the combustor was self-similar, regardless of the Reynolds number, Re of the operating ^{931} condition. Further, it was reported that the velocity decay was steeper for reacting ^{932} cases compared to non-reacting cases. ^{933}

The results presented in Figure FIXME however, show that even though Cases 1 ^{934} and 2 have similar Re, their mean velocity profiles have very different slopes. Further, ^{935} the reacting and non-reacting cases (both at preheated conditions) have similarly ^{936} steep slopes. This indicates that the mean axial stretch in the near field of the LSB ^{937} flow field is a stronger function of the preheat temperature than Re. The presence ^{938} of preheat results in increased viscosity that enhances the momentum transport in ^{939} the radial direction. This causes the velocity decay to be steep for preheated cases, ^{940} compared to cases without preheat. ^{941}

Assuming that S_T is constant, these results suggest that at higher preheat tem- ^{942} peratures, the flame would stabilize closer to the dump plane because of the faster ^{943} velocity decay and reduced local flow velocities. In fact, a faster velocity decay would ^{944} produce greater u' values and increase S_T, further causing the flame location to shift ^{945} upstream. Furthermore, in view of the steep velocity profile, it may be anticipated ^{946} that any changes in the stabilization location caused by perturbations in the local ^{947} flow field (and hence, the local turbulent flame propagation velocity) are likely to be ^{948} of diminished magnitude in the presence of preheat. All of this leads to an intuitive ^{949} result — the LSB flame behaves more stably at high preheat conditions. ^{950}

5.3 Effect of swirler vane angle

As described in Chapter FIXME 3, the LSB swirlers tested for this study are designed to have the same mass flow splits. The $S_{45°}$ swirler has a higher vane angle, resulting in greater blockage to the flow passing through the annular section. In order to compensate for this, the perforated plate covering the central section has slightly smaller holes. The net effect retains the same mass flow split as in the $S_{37°}$ swirler.

Chapter FIXME 2 describes how the swirler vane angle relates to the amount of swirl imparted to the incoming flow. According to Equation FIXME, a swirler with a higher vane angle will produce greater swirl in the reactants. Previous work in swirl combustion[26, 27] has pointed out that increased swirl shortens the flame by enhancing the swirl-induced radial pressure gradients. The data acquired in the present investigation is in agreement with this observation. Operated at identical inlet conditions, the $S_{45°}$ swirler stabilizes a flame closer to the dump plane and with a larger flame angle compared to the $S_{37°}$ swirler.

This result highlights an interesting trade-off for the designers of LSB-based gas turbine engines. The $S_{45°}$ flame is located further upstream and has a more concentrated region of heat release. This enhances the strength of the toroidal recirculation zone near the dump plane, which may be powerful enough under certain conditions (as we shall see in Section 5.4) to even cause the flame to attach itself to the lip of the inlet. All of this means that the $S_{45°}$ flame is more stable and will resist perturbations in the incoming flow better than the $S_{37°}$ flame. However, the presence of a strong recirculation zone in the flow field of the $S_{45°}$ swirler will entrain more hot products and retain them longer near the zone of heat release. This is a recipe for the production of thermal NO_x. While no emission measurements were made as part of this study, it may be reasonably anticipated that the NO_x performance of the $S_{45°}$ swirler will be degraded compared to the $S_{37°}$ swirler. The trade-off for gas turbine

engine designers is thus between flame stability and emissions performance. 977

5.4 Effect of equivalence ratio 978

The LSB is primarily intended for fuel-lean operation in order to utilize its low NO_x 979
emission performance. As a result, most of the testing was done as close as possible 980
to a target ϕ of 0.56. Limited testing was carried out at 12 atm for two off-target 981
conditions: a slightly richer ($\phi \approx 0.58$) and a slightly leaner ($\phi \approx 0.53$) mixture, in 982
order to explore the sensitivity of the LSB flame to limited changes in equivalence 983
ratio. The $S_{45°}$ swirler was used for these tests. The corresponding averaged and 984
Abel-deconvoluted flame images are presented in Figure FIXME. 985

Two characteristics of the flame are immediately obvious from these images. First, 986
the zone of heat release, marked by the region from which CH* chemiluminescence 987
is observed, is increasingly compact at fuel-rich conditions. Virtually all other flame 988
images acquired at a leaner condition show a long flame, with the heat release dis- 989
tributed over the entire visible area of the combustor. The compactness of the heat 990
release zone indicates potentially poor NO_x performance at these conditions. 991

Second, the fuel-rich flame brush can be observed to wrap around and anchor itself 992
on the dump plane. This is particularly observable in the Abel-deconvoluted image. 993
The attached region is not as bright as the rest of the flame brush, indicating that 994
the flame may be attaching itself intermittently. This intermittent behavior can be 995
confirmed from the instantaneous images where it is visible on some of the acquired 996
images, but not others. This behavior was alluded to in Section 5.3 as being the 997
result of the enhanced toroidal recirculation zone produced by this swirler. Thus, the 998
intermittent attachment of the flame to the inlet indicates the increased importance 999
of the toroidal recirculation zone in stabilizing the flame. 1000

It should be noted that the reliance on a toroidal recirculation zone to anchor 1001
the flame to the inlet is one of the primary flame stabilization mechanisms used by 1002

53

traditional swirl combustors. Thus, LSB swirlers with high vane angles tend to behave 1003
like traditional swirl combustors at fuel-rich conditions. 1004

5.5 Effect of combustor pressure 1005

In many gas turbine engines, the combustor pressure varies directly with the loading 1006
of the engine. Like the preheat temperature, the combustor pressure affects the LSB 1007
flame both through the fluid mechanics of the flow and the kinetics of the chemical 1008
reactions in the flame. The effect of the combustor pressure on the fluid mechanics 1009
of the LSB flow field can be captured by its effect on the Reynolds number. As noted 1010
in Section 5.2, however, previous work indicated the Reynolds number may not be 1011
an important parameter for the LSB, particularly in the near field where the flame 1012
stabilization occurs. On the other hand, the effect of the combustor pressure on reac- 1013
tion rates in the flame is clearly important. Increasing the combustor pressure results 1014
in a lower laminar flame speed and reduced flame thickness for methane-air flames. 1015
According to the modified Damköhler model discussed earlier, the reduced laminar 1016
flame speed should have little or no effect on the flow field, since the contribution from 1017
S_L in Equation FIXME is vanishingly small, even at the lowest reference velocities 1018
of our test conditions. However, as suggested by our discussion in Section 5.1, the 1019
validity of the simple model at elevated pressure conditions is questionable. 1020

In order to resolve the uncertainties regarding how the LSB flame responds to 1021
combustor pressure, the flame was imaged over a range of operating conditions from 1022
3 to 12 atm. For these tests, the reference velocity and the equivalence ratio were 1023
held constant. However, the temperature of the reactants continues to increase with 1024
pressure. The reason for this was discussed in Chapter FIXME 3 and is attributable 1025
to the reduced heat losses in the connecting pipes at the high flow rates required to 1026
pressurize the LSB. The flame location and shape inferred from the flame images are 1027
presented in Figure FIXME. 1028

At low to moderate pressures, the flame location is nearly invariant for S_{37°, but moves upstream for the S_{45° cases. This behavior can be explained as follows. The flame stabilization location for the S_{45° swirler is closer to the dump plane compared to the S_{37° swirler. This should result in enhanced heat transfer to the dump plane and consequently to the incoming reactants. This feedback is even more effective as the temperature of the incoming reactants increases. This causes the upstream shift of the S_{45° flame, while the S_{37° flame is less affected by these processes.

At high pressures, however, both flames are observed to move downstream, despite the increasing preheat temperatures. The apparent decrease in the turbulent flame speed at these conditions is an unexpected result, and the modified Damköhler model is insufficient in accounting for this observation. Figure FIXME also shows that the flame angle for both cases decreases slightly with pressure. This suggests that the turbulent flame speed was consistently decreasing with pressure. In light of this, the nearly constant location of the S_{37° flame could be attributed to the effects of increasing combustor pressure and preheat temperature nearly canceling each other out at the lower pressures.

5.6 Flame structure

CHAPTER 6

CONCLUSIONS

APPENDIX A

SEEDER DESIGN

A new seeder was designed for use in high pressure implementations of diagnostic techniques like Laser Doppler Velocimetry (LDV), Particle Image Velocimetry (PIV), etc.

The previous design, as shown in Figure A.1, was a fluidized bed seeding generator. Seeding particles in a cylindrical vessel are fluidized by an air-turbine vibrator. Air is introduced into the vessel in the form of two opposing jets directed tangentially to produce a small amount of swirl in the flow field. Particles are picked up by the air flow and the swirl aids in separating the heavy/coagulated clumps of seeding particles by centrifugal acceleration.

This design had several shortcomings. First, it is observed that the seeding density of the seeded flow generally decreases over time, even if the seeding particles have not been depleted. The seeding particles tend to coagulate over time, due to the buildup of moisture, static charge, etc. In such cases, the vibrator can no longer effectively fluidize the particles. Further, the tangential introduction of the air flow preferentially depletes particles near the walls of the container, leaving the center relatively undisturbed. The cumulative effect of these phenomena diminishes the effectiveness of the seeder.

Second, the fluidized bed requires a minimum amount of seeding particles to function effectively. This requires the seeder to be refilled even before all the seeding particles are consumed.

Third, when designed for high pressure applications, the seeder will become quite heavy due to flanges and other fittings. Such a setup cannot be easily fluidized using a reasonable-sized air-turbine vibrator.
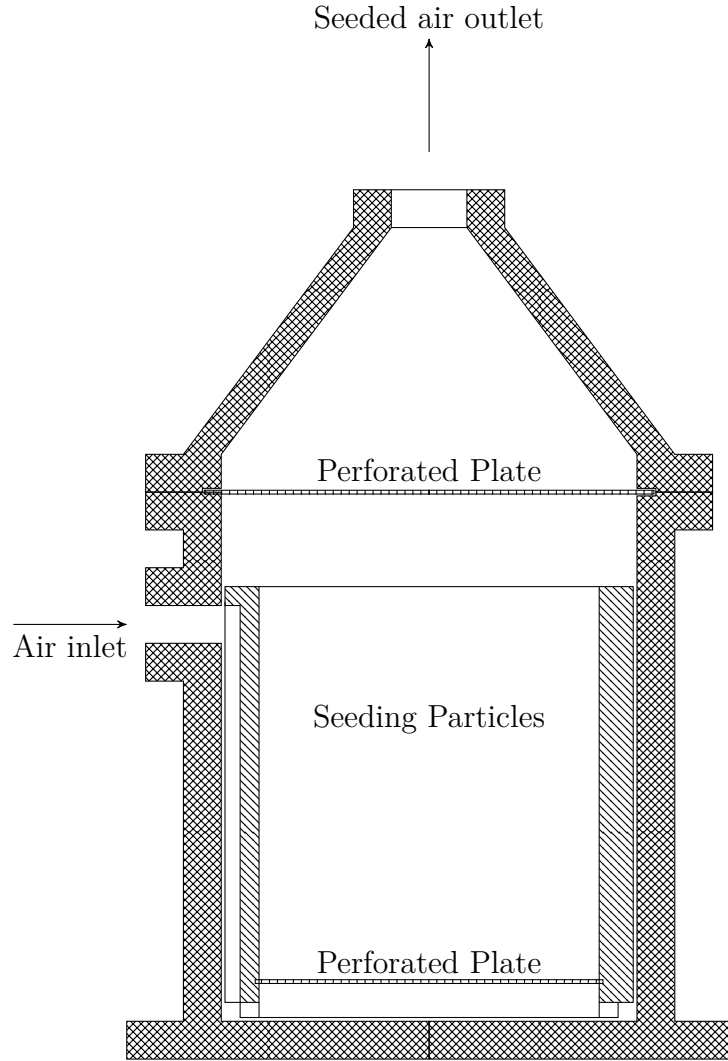
Figure A.1: *A schematic of the old fluidized bed seeder is presented. The air enters the seeder through a groove along the inner vessel and is injected with a tangential velocity at the base of the seeder. The whole assembly is vibrated (vibrator not shown) to keep the particle bed fluidized. The seeded air flow exits through the outlet on the top.*

Seeded air outlet

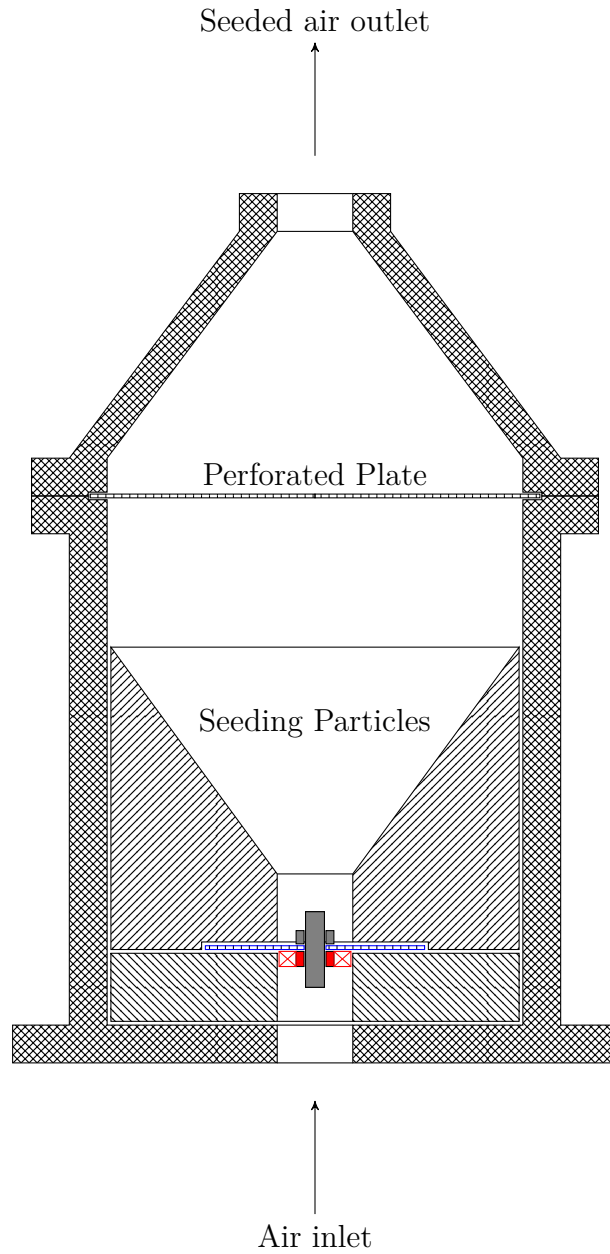Perforated Plate

Seeding Particles

Air inlet

Figure A.2: *The improved design of the seeder is shown here in schematic form. The air enters the assembly from the inlet at the bottom, passes through the swirler (shown in red) and enters the seeder. The perforated plate at the bottom (shown in blue) keeps the seeding particles within the seeder. The swirler hub is threaded, allowing it to be secured to the perforated plate by a short steel bolt (shown in gray). After picking up the particles, a second perforated plate prevents large clumped seeding particles from passing through. The seeded air flow exits through the outlet at the top.*

The new seeder design is shown in Figure A.2, and resembles a funnel with a swirler located halfway up the stem. A perforated base plate holds the swirler and the seeding particles in the conical section of the swirler. Due to the steep angle of the sides of the conical section, the seeding particles continuously collapse into the central section. This negates any need for vibrating the system. Air is introduced from the bottom of the seeder and enters the vessel by passing through the swirler. Since all the air enters this way, there is a considerable amount of swirl in the resulting flow field, Heavy/coagulated seeding particles are flung outward, while lighter particles are carried with the air. After a sufficient distance to allow for the cyclonic separation to be effective, the seeded air passes through another perforated plate which further limits the presence of large clumps of particles. The exiting air is now spatially and temporally uniformly seeded.

REFERENCES

[1] C. M. Vagelopoulos and J. H. Frank, "An experimental and numerical study on the adequacy of CH as a flame marker in premixed methane flames," in *Proceedings of the Combustion Institute*, vol. 30, pp. 241–249, 2005.

[2] M. Köhler, A. Brockhinke, M. Braun-Unkhoff, and K. Kohse-Höinghaus, "Quantitative Laser Diagnostic and Modeling Study of C_2 and CH Chemistry in Combustion," *The Journal of Physical Chemistry A*, vol. 114, no. 14, pp. 4719–4734, 2010.

[3] C. P. Fenimore, "Formation of nitric oxide in premixed hydrocarbon flames," in *Symposium (International) on Combustion*, vol. 13, pp. 373–380, 1971.

[4] R. S. Barlow, R. W. Dibble, J. Y. Chen, and R. P. Lucht, "Effect of Damköhler Number on Superequilibrium OH Concentration in Turbulent Nonpremixed Jet Flames," *Combustion and Flame*, vol. 82, no. 3-4, pp. 235–251, 1990.

[5] C. F. Kaminski, J. Hult, and M. Aldén, "High repetition rate planar laser induced fluorescence of OH in a turbulent non-premixed flame," *Applied Physics B: Lasers and Optics*, vol. 68, no. 4, pp. 757–760, 1999.

[6] J. Hult, U. Meier, W. Meier, A. Harvey, and C. F. Kaminski, "Experimental analysis of local flame extinction in a turbulent jet diffusion flame by high repetition 2-D laser techniques and multi-scalar measurements," in *Proceedings of the Combustion Institute*, vol. 30, pp. 701–709, 2005.

[7] H. Malm, G. Sparr, J. Hult, and C. F. Kaminski, "Nonlinear diffusion filtering of images obtained by planar laser-induced fluorescence spectroscopy," *Journal*

1086
1087
1088
1089
1090
1091
1092
1093
1094
1095
1096
1097
1098
1099
1100
1101
1102
1103
1104
1105
1106

of The Optical Society of America A: Optics, image science, and vision, vol. 17, no. 12, pp. 2148–2156, 2000.

[8] R. Abu-Gharbieh, G. Hamarneh, T. Gustavsson, and C. F. Kaminski, "Flame front tracking by laser induced fluorescence spectroscopy and advanced image analysis," *Optics Express*, vol. 8, no. 5, pp. 278–287, 2001.

[9] H. N. Najm, P. H. Paul, C. J. Mueller, and P. S. Wyckoff, "On the Adequacy of Certain Experimental Observables as Measurements of Flame Burning Rate," *Combustion and Flame*, vol. 113, no. 3, pp. 312–332, 1998.

[10] J. Kiefer, Z. S. Li, J. Zetterberg, X. S. Bai, and M. Aldén, "Investigation of local flame structures and statistics in partially premixed turbulent jet flames using simultaneous single-shot CH and OH planar laser-induced fluorescence imaging," *Combustion and Flame*, vol. 154, no. 4, pp. 802–818, 2008.

[11] P. H. Paul and H. N. Najm, "Planar laser-induced fluorescence imaging of flame heat release rate," in *Symposium (International) on Combustion*, vol. 27, pp. 43–50, 1998.

[12] J. Kiefer, Z. S. Li, T. Seeger, A. Leipertz, and M. Aldén, "Planar laser-induced fluorescence of HCO for instantaneous flame front imaging in hydrocarbon flames," in *Proceedings of the Combustion Institute*, vol. 32, pp. 921–928, 2009.

[13] Z. S. Li, J. Kiefer, J. Zetterberg, M. Linvin, A. Leipertz, X. S. Bai, and M. Aldén, "Development of improved PLIF CH detection using an Alexandrite laser for single-shot investigation of turbulent and lean flames," in *Proceedings of the Combustion Institute*, vol. 31, pp. 727–735, 2007.

[14] J. Luque and D. R. Crosley, "Electronic transition moment and rotational transition probabilities in CH. II. $B^2\Sigma^- - X^2\Pi$ system," *Journal of Chemical Physics*, vol. 104, no. 11, pp. 3907–3913, 1996.

[15] N. L. Garland and D. R. Crosley, "Energy transfer processes in CH $A^2\Delta$ and $B^2\Sigma^-$ in an atmospheric pressure flame," *Applied Optics*, vol. 24, no. 23, pp. 4229–4237, 1985.

[16] J. Luque, R. J. H. Klein-Douwel, J. B. Jeffries, and D. R. Crosley, "Collisional processes near the CH $B^2\Sigma^- v' = 0, 1$ predissociation limit in laser-induced fluorescence flame diagnostics," *Applied Physics B: Lasers and Optics*, vol. 71, no. 1, pp. 85–94, 2000.

[17] J. W. Daily, "Laser induced fluorescence spectroscopy in flames," *Progress in Energy and Combustion Science*, vol. 23, no. 2, pp. 133–199, 1997.

[18] M. Zachwieja, "New Investigations of the $A^2\Delta - X^2\Pi$ Band System in the CH Radical and a New Reduction of the Vibration-Rotation Spectrum of CH from the ATMOS Spectra," *Journal of Molecular Spectroscopy*, vol. 170, no. 2, pp. 285–309, 1995.

[19] J. Luque and D. R. Crosley, "Electronic transition moment and rotational transition probabilities in CH. I. $A^2\Delta - X^2\Pi$ system," *Journal of Chemical Physics*, vol. 104, no. 6, pp. 2146–2155, 1996.

[20] D. T. Yegian and R. K. Cheng, "Development of a lean premixed low-swirl burner for low NO_x practical applications," *Combustion Science and Technology*, vol. 139, no. 1, pp. 207–227, 1998.

[21] A. Marshall, P. Venkateswaran, D. Noble, J. Seitzman, and T. Lieuwen, "Development and characterization of a variable turbulence generation system," *Experiments in Fluids*, vol. 51, no. 3, pp. 611–620, 2011.

[22] A. Melling, "Tracer particles and seeding for particle image velocimetry," *Measurement Science and Technology*, vol. 8, no. 1, pp. 1406–1416, 1997.

[23] Y. Hardalupas, C. S. Panoutsos, and A. M. K. P. Taylor, "Heat Release Rate Measurements in Premixed Flames using Chemiluminescence and Reaction Rate Imaging," in *44th AIAA Aerospace Sciences Meeting and Exhibit, Reno, NV, January 9–12*, 2006.

[24] C. J. Dasch, "One-dimensional tomography: a comparison of abel, onion-peeling, and filtered backprojection methods," *Applied Optics*, vol. 31, no. 8, pp. 1146–1152, 1992.

[25] R. K. Cheng, D. Littlejohn, W. A. Nazeer, and K. O. Smith, "Laboratory Studies of the Flow Field Characteristics of Low-Swirl Injectors for Adaptation to Fuel-Flexible Turbines," *Journal of Engineering for Gas Turbines and Power*, vol. 130, p. 021501, 2008.

[26] C. K. Chan, K. S. Lau, W. K. Chin, and R. K. Cheng, "Freely propagating open premixed turbulent flames stabilized by swirl," in *Symposium (International) on Combustion*, vol. 24, pp. 511–518, 1992.

[27] S. H. Stårner and R. W. Bilger, "Joint measurements of velocity and scalars in turbulent diffusion flame with moderate swirl," in *Symposium (International) on Combustion*, vol. 21, pp. 1569–1577, 1986.